Analysis of Mass Transfer in a Corotating Disks Catalytic Reactor

Clara-Tatiana Gonzalez-Hidalgo and Joan Herrero
Dept. Enginyeria Quimica, ETSEQ, Universitat Rovira i Virgili, Tarragona, Catalonia, Spain

Dolors Puigjaner
Dept. Enginyeria Informàtica i Matemàtiques, ETSE, Universitat Rovira i Virgili, Tarragona, Catalonia, Spain

DOI 10.1002/aic.14668
Published online November 15, 2014 in Wiley Online Library (wileyonlinelibrary.com)

The flow and mass transfer in a discontinuous reactor configuration consisting of a pair of corotating enclosed disks with a chemical reaction taking place at the disk surfaces have been analyzed. The calculated mass-transfer efficiencies do not follow the expected $Sh=Sh(Re,Sc)$ dependence because the overall mass-transfer process is not boundary-layer controlled, especially at high Schmidt numbers. It has been found in all of the cases investigated that despite the fact that the reactant concentration is continuously dropping with time its spatial distribution, relative to the volume-averaged value, becomes stationary after a short initial transient. This result implies that the mass-transfer efficiency in the discontinuous reactor also becomes stationary and the resulting time-independent value, Sh_∞, obtained either directly from calculation or from the fit of the collected results, provides a fairly good estimate of the reactor operation time needed to achieve the target reactant conversion. © 2014 American Institute of Chemical Engineers *AIChE J*, 61: 1015–1031, 2015

Keywords: mass transfer, mixing, computational fluid dynamics, numerical solutions

Introduction

The determination of conditions that most reduce mass-transfer resistance is a fundamental issue for the enhancement of productivity in chemical reactors. One way to promote mixing is by means of a forced convection flow that facilitates transport of the reactant (product) toward (from) the catalytic surface.[1–4] For example, Al-Shannag et al.[3] proposed and analyzed a heterogeneous catalytic reactor in a cavity of square cross-section where mixing was promoted by the sliding top lid. Al-Shannag[4] showed that a similar setup in a toroidally shaped cavity of square cross-section yielded higher mixing efficiencies. In a recent work,[5] we proposed and analyzed a catalytic reactor of cubical shape where flow was driven by natural convection. This kind of reactor, which avoids the use of mechanical devices to promote mixing, is specially suitable for enzymatic reactions where high levels of shear stress are undesirable. The overall mass-transfer process between the reactor bulk and the wall surface with the implanted catalyst was found to be controlled by the rate of mass transfer within the concentration boundary layer. Although the reactor investigated in Ref. 5 is quite efficient in terms of mass-transfer rates, it is suitable only for small volumes, slow reactions, and aqueous solutions. The present investigation aims to widen our scope to deal with bigger reaction volumes and either a liquid or a gas phase.

Correspondence concerning this article should be addressed to C. Gonzalez at claratatiana.gonzalez@urv.cat.

A good deal of technological applications involve heat or mass transfer between the surface of a rotating disk and the surrounding fluid. As an example, Drumm et al.[6,7] studied numerically and experimentally liquid-liquid extraction in a column where several rotating disks acted as stirrers. As a filtration process application, Francis et al.[8] analyzed a controlled-shear affinity filtration process where a rotor is positioned above a membrane to allow protein capture and purification from cell culture. The application of rotating disk systems to chemical reactors is extensive, a few representative examples will be cited in what follows. Zhang et al.[9] studied the effect of the disk rotation speed on the growth of ZnO films, used in light emitting diodes and laser diodes, by metal–organic chemical vapor deposition. Meeuwse et al.[10,11] investigated the gas-liquid and liquid-solid mass transfer in a rotor–stator spinning disk equipment. Visscher et al.[12] measured the liquid-liquid mass transfer in the same rotor–stator device. In the three latter cases, the aim of the authors was to attain mass-transfer efficiency levels comparable to those typically achieved in more traditional reactors. Leon et al.[13] described an horizontal rotating foam reactor where the foam structures are used as stirrers that mix the components and disperse fine bubbles. Belfiore et al.[14] and Belfiore[15] investigated the application of rotating disks to biological reactors. These authors studied the response of dynamic shear in a continuous flow corotating disk catalytic reactor. Belfiore et al.[14] found that the dynamic shear has an important effect only above a critical stress-sensitive Damköhler number. Belfiore[15] found that chemical reaction was enhanced by viscous shear at the interface between the bulk fluid and the rotating plate.

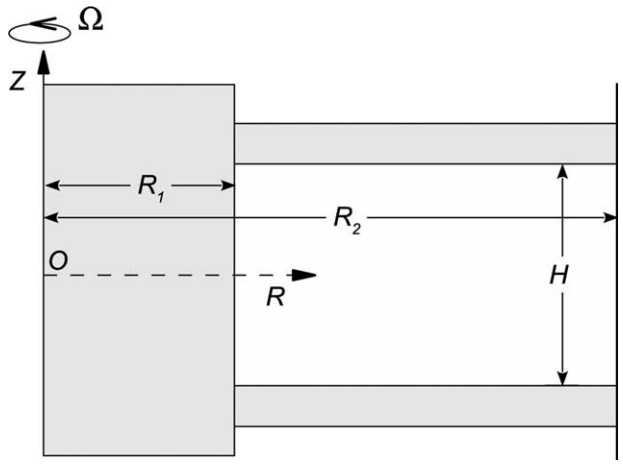

Figure 1. Sketch of the corotating disk reactor geometry.

Since axisymmetry is assumed only the reactor projection into the radial-axial (*R*,*Z*) plane is shown.

The reactor setup that is analyzed numerically in this study is sketched in Figure 1. It consists of a pair of corotating disks enclosed by a cylindrical container at rest. The inner surfaces of both disks are coated with a layer of catalyst where a first-order chemical reaction takes place. It is worth pointing out that a catalytic reactor in a similar geometry, a single rotating enclosed disk, was investigated experimentally by Meeuwse et al.[11] The system of Figure 1 can be understood as a simplified model of a more complex setup with a stack of several corotating disks once the interactions between contiguous interdisk spaces are dismissed.

The flow between two corotating disks attracted considerable research interest[16–24] as a simple model that captured most of the basic features of the flow of air inside computer hard disks devices. It is well-known that the rotation of the disks produces a secondary flow in the cross-stream plane with fluid moving outward along the boundary layer region close to each disk surface. At low Reynolds numbers, the flow is steady and axisymmetric (2-D), that is, independent of the angular coordinate θ, and the cross-stream vortices resemble those found in the Taylor–Couette flow.[25]

In the current problem, we will focus on the analysis of a reactor operating in discontinuous (batch) mode. Batch reactors are widely used in the food and pharmaceutical industries and, in general, in those processes where a particular reactor unit is used to manufacture relatively small amounts of different products (or a product having various flavors: pigments, additives, etc.). They are also of common use at the laboratory level when, for example, the kinetics of a given chemical reaction or the performance of a new catalyst have to be investigated. The range of the problem parameters currently investigated might be realized, in a practical application, in a reactor having a volume of about 1 L with the disks, about 0.05–0.10 m in diameter, spinning in the range of $\Omega \leq 200\ \pi$ rad/s for gas-phase operation and $\Omega \leq 20\ \pi$ rad/s for a liquid phase. It is important to note that in the liquid-phase case, the numerical analysis of the mass-transfer problem is especially challenging because of the high values of the Schmidt number involved. This is the reason why a highly accurate Galerkin spectral discretization of the conservation partial differential equations has been used. The main goal of this study is to solve the governing equations numerically and then to analyze the results to establish the dependence of the mass-transfer efficiency on the problem parameters (Reynolds, Schmidt, and Damköhler numbers and height to radius aspect ratio). Special attention will be given to the prediction of the operation time required to achieve a target conversion, a quantity of utmost importance in batch operation.

Problem Formulation

Fluid mechanics model

The Newtonian laminar flow in a catalytic chemical reactor was investigated. The reactor, which is sketched in Figure 1, consists of two coaxial disks attached to and corotating with a hub enclosed in a cylindrical cavity at rest. The velocity and concentration fields are assumed to be axisymmetric, that is, velocity and concentration depend only on the radial (R) and axial (Z) cylindrical coordinates. Under the aforementioned assumptions, the mass and momentum dimensionless conservation equations for the velocity (U, V, W) and pressure P may be written, in a frame of reference rotating at the angular velocity Ω, as

Mass

$$\frac{1}{S}\frac{\partial W}{\partial Z}+\frac{\partial U}{\partial R}+\frac{U}{R}=0 \tag{1}$$

Radial momentum

$$\frac{\partial U}{\partial \tau}+\frac{W}{S}\frac{\partial U}{\partial Z}+U\frac{\partial U}{\partial R}=-\frac{\partial P}{\partial R}+\frac{1}{Re}\left\{\frac{\partial}{\partial R}\left(\frac{1}{R}\frac{\partial}{\partial R}[RU]\right)+\frac{1}{S^2}\frac{\partial^2 U}{\partial Z^2}\right\}+\left(2V+\frac{V^2}{R}+R\right) \tag{2}$$

Circumferential momentum

$$\frac{\partial V}{\partial \tau}+\frac{W}{S}\frac{\partial V}{\partial Z}+U\frac{\partial V}{\partial R}=+\frac{1}{Re}\left\{\frac{\partial}{\partial R}\left(\frac{1}{R}\frac{\partial}{\partial R}[RV]\right)+\frac{1}{S^2}\frac{\partial^2 V}{\partial Z^2}\right\}-\left(2U+\frac{UV}{R}\right) \tag{3}$$

Axial momentum

$$\frac{\partial W}{\partial \tau}+\frac{W}{S}\frac{\partial W}{\partial Z}+U\frac{\partial W}{\partial R}=-\frac{1}{S}\frac{\partial P}{\partial Z}+\frac{1}{Re}\left\{\frac{1}{R}\frac{\partial}{\partial R}\left(R\frac{\partial W}{\partial R}\right)+\frac{1}{S^2}\frac{\partial^2 W}{\partial Z^2}\right\} \tag{4}$$

Note that in the rotating frame of reference, the circumferential component of velocity, V, vanishes at the hub and disk surfaces, thus boundary conditions for Eqs. 1–4 are

$$U=V=W=0 \quad \text{at} \quad Z=\pm 1/2 \quad \text{or} \quad R=\gamma \tag{5}$$

$$U=W=0, V=-1 \quad \text{at} \quad R=1 \tag{6}$$

The rightmost term R in Eq. 2 denotes the centrifugal force while the terms $2V$ and $-2U$ within the rightmost parenthesis in Eqs. 2 and 3 are the respective components of the Coriolis force. Length and velocity scales used to obtain the dimensionless variables, R, Z, U, V, and W, in Eqs. 1–6 are R_2, H, and ΩR_2, respectively. The dimensionless time (τ) has been defined on the basis of the diffusive time $t_C=R_2^2/D$ with D

being the binary coefficient of molecular diffusion for the reactant/solvent pair. The mass and momentum conservation problem 1–6 is, therefore, determined by the values of three dimensionless parameters, namely the Reynolds number, Re, the height to outer radius ratio, S, and the radius ratio, γ. These parameters are defined as $Re=\Omega R_2^2/\nu$ (ν denotes the kinematic viscosity of the fluid), $S=H/R_2$ and $\gamma=R_1/R_2$. Note that the latter quantity only appears explicitly in the boundary condition 5 at the rotating hub surface.

Instead of solving the mass and momentum conservation equations in terms of velocity and pressure, we used the axisymmetric velocity potential, Ψ, also known as streamfunction

$$U=-\left(\frac{1}{R}\right)\frac{\partial\Psi}{\partial Z} \tag{7}$$

$$W=\left(\frac{S}{R}\right)\frac{\partial\Psi}{\partial R} \tag{8}$$

It is clear that when Eqs. 7 and 8 are used, the continuity equation 1 is automatically fulfilled. Boundary conditions 5 and 6 may be, therefore, written as

$$V=\frac{\partial\Psi}{\partial Z}=\frac{\partial\Psi}{\partial R}=0 \quad \text{at} \quad Z=\pm\frac{1}{2} \quad \text{or} \quad R=\gamma \tag{9}$$

$$V=-1, \quad \frac{\partial\Psi}{\partial Z}=\frac{\partial\Psi}{\partial R}=0 \quad \text{at} \quad R=1 \tag{10}$$

Note that since Ψ must be continuous along the boundary, Eqs. 9 and 10 can be replaced by

$$V=\Psi=\frac{\partial\Psi}{\partial Z}=0 \quad \text{at} \quad Z=\pm\frac{1}{2} \tag{11}$$

$$V=\Psi=\frac{\partial\Psi}{\partial R}=0 \quad \text{at} \quad R=\gamma \tag{12}$$

$$V=-1, \quad \Psi=\frac{\partial\Psi}{\partial R}=0 \quad \text{at} \quad R=1 \tag{13}$$

Mass-transfer model

The dimensionless conservation equation for the molar concentration, $C(\tau,R,Z)$, of the reactant species can be written as

$$\frac{\partial C}{\partial\tau}=\left[\frac{1}{R}\frac{\partial C}{\partial R}+\frac{\partial^2 C}{\partial R^2}+\frac{1}{S^2}\frac{\partial^2 C}{\partial Z^2}\right]-ReSc\left[U\frac{\partial C}{\partial R}+W\frac{1}{S}\frac{\partial C}{\partial Z}\right] \tag{14}$$

where $Sc=\nu/D$ is the Schmidt number. The catalytic reaction is assumed to take place on the surfaces of the corotating disks, whereas both the surface of the rotating hub and the outer cylindrical enclosure wall are assumed to be impermeable. Thus, boundary conditions for Eq. 14 are

$$\frac{\partial C}{\partial Z}=\pm\phi C \quad \text{at} \quad Z=\mp\frac{1}{2} \tag{15}$$

$$\frac{\partial C}{\partial R}=0 \quad \text{at} \quad R=\gamma,1 \tag{16}$$

where ϕ is the Damköhler number defined as $\phi=kH/D$, being k the constant of the first-order law for the rate of chemical reaction per unit area.

Problem scaling

The Damköhler number, $\phi=kH/D$, is usually interpreted as the ratio of the rate of chemical reaction at the catalyst surface to the rate of mass transfer by molecular diffusion. As can be easily deduced from Eq. 14, the quantity $ReSc$, known as the Péclet number, Pe, gives a ratio between characteristic times for molecular diffusion and convection of the reactant species. Thus, one would expect that the rate of convection provided by the corotating disks system will be fast enough to achieve a good mixing, whenever $Pe\gg\phi$. At a quantitative level, the mixing capability of the system is often measured in terms of the mass-transfer efficiency, η. This quantity is defined as the ratio of the average rate of reaction at the catalytic surface to the maximum value of the average rate of reaction, that is, the one value that would be only attained in the ideal perfect mixing limit

$$\eta(\tau)=\frac{k\hat{C}(\tau,\pm1/2)}{k\bar{C}(\tau)}=\frac{2k\int_\gamma^1 C(\tau,R,\pm1/2)RdR/(1-\gamma^2)}{2k\int_{-1/2}^{1/2}\int_\gamma^1 C(\tau,R,Z)RdRdZ/(1-\gamma^2)} \tag{17}$$

Mass-transfer efficiency can also be characterized in terms of the Sherwood number, $Sh(\tau)=\hat{K}(\tau)R_2/D$, where $\hat{K}(\tau)$ denotes the surface averaged convective mass-transfer coefficient defined by

$$k\hat{C}(\tau,\pm1/2)=\hat{K}(\tau)\left[\bar{C}(\tau)-\hat{C}(\tau,\pm1/2)\right] \tag{18}$$

Let S denotes the height to outer radius ratio, $S=H/R_2$. The Sherwood number and the reactor efficiency, $\eta(\tau)$, are therefore related by

$$Sh(\tau)=\frac{\hat{K}(\tau)R_2}{D}=\left(\frac{1}{S}\right)\frac{\phi\hat{C}(\tau,\pm1/2)/\bar{C}(\tau)}{1-\hat{C}(\tau,\pm1/2)/\bar{C}(\tau)}=\frac{\phi\eta(\tau)}{S[1-\eta(\tau)]} \tag{19}$$

$$\eta(\tau)=\frac{Sh(\tau)}{\left(\frac{\phi}{S}\right)+Sh(\tau)} \tag{20}$$

It is also common to consider the dimensionless overall mass-transfer coefficient, $Sh_{\mathrm{OV}}(\tau)$

$$\frac{1}{Sh_{\mathrm{OV}}(\tau)}=\frac{1}{Sh(\tau)}+\frac{S}{\phi}=\frac{S}{\phi}\left[\frac{1-\eta(\tau)}{\eta(\tau)}+1\right]=\frac{S}{\phi\eta(\tau)} \tag{21}$$

Note that Eq. 21 assumes an overall resistance to mass transfer $(1/Sh_{\mathrm{OV}})$ that is composed of two different contributions. The term $(1/Sh)$ characterizes resistance to mass transfer by combined diffusion plus convection, whereas the term (S/ϕ) represents the resistance associated with the chemical reaction at the catalyst surface. If the surface reaction is a slow one, small ϕ, we should expect $S/\phi\gg1/Sh(\tau)$ in Eq. 21, and therefore, values of $\eta(\tau)$ close to one would be attained on account of Eq. 20. In the opposite situation, a fast reaction yielding a large ϕ value, we have $S/\phi\ll1/Sh(\tau)$), that is, convection plus molecular diffusion control the overall mass-transfer process thus yielding low values of $\eta(\tau)$.

The question is how to quantify the above qualitative trends, that is, how close to one (zero) will be $\eta(\tau)$ when ϕ takes a small (large) value. Therefore, much attention will be devoted to the relation between the reactor mass-transfer efficiency and the parameters of the problem, S, Re, Sc, and ϕ. In particular, if the overall process of reactant transfer into the catalytic surface is to be controlled by molecular diffusion within a boundary layer region then one would expect the Sherwood number to depend on a product of

powers of S, Re, and Sc. This was indeed the case in the natural convection-driven catalytic reactor that we analyzed in Ref. 5 but, as will be seen below, things are not that simple in the current problem.

Numerical Method

Velocity field

In this work, it is assumed that the concentration levels of the solute, C, are much lower that the concentration of the mixture. Consequently, it is assumed that fluid properties, and more specifically the kinematic viscosity, ν, are constant. The fluid mechanics problem 1–6 is, therefore, independent of the mass-transfer problem 14–16. Note that since the characteristic time for the fluid mechanics problem 1–6 is $t_U = R_2^2/\nu$ then $t_U/t_C = D/\nu = 1/Sc$. Thus, a large Sc value implies a low value of the t_U/t_C ratio. The implication at the numerical level is that to solve Eqs. 1–6 and 14–16 together the number of time steps would be about Sc times larger than it is when only Eqs. 14–16 are advanced in time. This would make the numerical solution of the fully coupled problem exceedingly expensive, whenever $Sc \gg 1$. In practice, the assumption of constant ν would hold, for example, for systems like the one used in Ref. 11, where oxygen was dissolved in a liquid solution. More generally, the current uncoupled model would be appropriate whenever variations on the concentration levels of reactants and products do not significantly alter the density or the viscosity of the mixture.

In addition, only steady-state solutions are considered, and therefore, the time derivative in the left-hand side of 2–4 vanishes. The steady flow assumption is reasonable in the range of low to moderate Reynolds numbers investigated, $10^3 \le Re \le 10^5$, even though the real flow would probably be three-dimensional (3-D) in the uppermost part of this Re range. The introduction of the streamfunction Ψ defined by 7 and 8 in the steady-state version of 1–4 reduces the number of dependent variables from four (U, V, W, P) to three (Ψ, V, P). The resulting system of partial differential equations was discretized by means of a spectral tau–Galerkin method also known as Galerkin method with boundary bordering.[26] The streamfunction Ψ and the velocity V were expanded in terms of Chebyshev polynomials

$$\Psi(R,Z) = \sum_{i=4}^{N_{R,\Psi}} \sum_{j=4}^{N_{Z,\Psi}} \psi_{ij} f_i(R^*) f_j(Z^*) \tag{22}$$

$$V(R,Z) = \sum_{i=0}^{N_{R,V}} \sum_{j=0}^{N_{Z,V}} v_{ij} T_i(R^*) T_j(Z^*) \tag{23}$$

In expansions 22 and 23 $Z^* = 2Z$, $R^* = 2[(R-\gamma)/(1-\gamma) - 1/2]$, T_i denotes the Chebyshev polynomials of order i and f_i are suitable linear combinations of Chebyshev polynomials that satisfy $f_i(\pm 1) = f_i'(\pm 1) = 0$. This choice of the basis functions results in the automatic fulfillment of boundary conditions 11–13 for Ψ. As a consequence, no expansion is needed for the pressure, P, because the pressure gradient terms in 2 and 4 vanish when these equations, as an essential part of the Galerkin method, are projected into the subspace of the basis functions used in the Ψ expansion 22. Thus, the Galerkin projection yields a system of nonlinear algebraic equations whose unknowns are the ψ_{ij} and v_{ij} coefficients in the expansions 22 and 23. This system of equations was solved by means of the Newton iterative method.

A special treatment is needed to deal with the discontinuity in the boundary conditions for V at the external enclosure corners. That is, boundary conditions for V in 11 and 13 do not match as $0 = V(1, \pm 1/2) = -1$ is obviously impossible. Hence, the boundary condition $V(R, \pm 1/2) = 0$ was replaced in (11) by the following exponential function along the disk surfaces

$$V(R, \pm 1/2) = -(1+\zeta) \exp\left[\frac{-\ln(V_{res})}{\zeta}(R-1-\zeta)\right] \tag{24}$$

Equation 24 was inspired by the treatment of a similar velocity discontinuity at a boundary in a previous work by Lopez and Shen,[27] which was later applied[28] to the calculation of the flow inside an annular container with a rotating bottom lid and inner cylinder. The idea behind the particular form of Eq. 24 is that at a small dimensionless radial distance ζ from the outer enclosure wall the velocity V should already have attained a residual value. In particular, at the disk tip, $R = 1$, Eq. 24 yields $V = -(1+\zeta)V_{\text{res}}$. In all of the calculations discussed below, we used $V_{\text{res}} = 10^{-3}$ and $\zeta = 0.05$. The influence of the ζ value on the numerical results will be assessed in the next section. To implement the modified boundary condition (24), the radial span $R \in [\gamma, 1]$ was extended to $R \in [\gamma, 1+\zeta]$ in Eqs. 1–6 as well as in the molar conservation model 14–16 and in the definition of R^*.

The use of the V boundary condition 24 is justified on physical grounds by the fact that $\zeta = 0$ is unattainable in a experimental equipment. From a theoretical point of view, it is known that in the limit case with $\zeta \to 0$, a very large number of functions ($N_{R,V} \to \infty$) would be needed in expansion 23 to properly characterize the problem. When the current $V_{\text{res}} = 10^{-3}$ and $\zeta = 0.05$ values were used in Eq. 24, it was numerically found that the required increase in the maximum polynomial degree reduced to $N_{R,V} = N_{R,\Psi} + 20$. When values of $N_{R,V} < N_{R,\Psi} + 20$ were used, the resulting V velocity fields turned out to be somewhat wiggly in the vicinity of the disk surfaces, $Z = \pm 1/2$. Furthermore, in all of the cases investigated, we set identical values of the truncation parameters for the axial direction in expansions 22 and 23, that is, $N_{Z,\Psi} = N_{Z,V}$.

Concentration field

Once the velocity field was obtained the solute conservation equation 14 was also solved by means of a spectral tau–Galerkin method.[26] Thus, using the concentration expansion

$$C(\tau,R,Z) = \sum_{i=0}^{N_R} \sum_{j=0}^{N_Z} c_{ij}(\tau) T_i(R^*) T_j(Z^*) \tag{25}$$

the application of the tau–Galerkin method reduces Eqs. 14–16 into a system of ordinary differential equations (ODEs) that can be written as

$$\hat{\mathbf{B}}\dot{\mathbf{c}} = \hat{\mathbf{L}}c + \hat{\mathbf{A}} \tag{26}$$

The vector $\mathbf{c}$ and the matrices $\hat{\mathbf{B}}, \hat{\mathbf{L}}$, and $\hat{\mathbf{A}}$ in 26 are defined in Appendix where the spatial discretization of the problem is detailed. The initial condition ($\tau = 0$) for the ODE system 26 is that the reactant species is perfectly well-mixed through all of the volume with an arbitrary concentration level equal to one. It should be, however, noted that, whereas boundary conditions 16 allow for a uniform radial distribution of C, a flat axial distribution, $C(0,R,Z) = 1$, would be incompatible with 15 (or, in other words, it is impossible to accurately project a step-like function into a polynomial basis). To overcome this technical difficulty, we

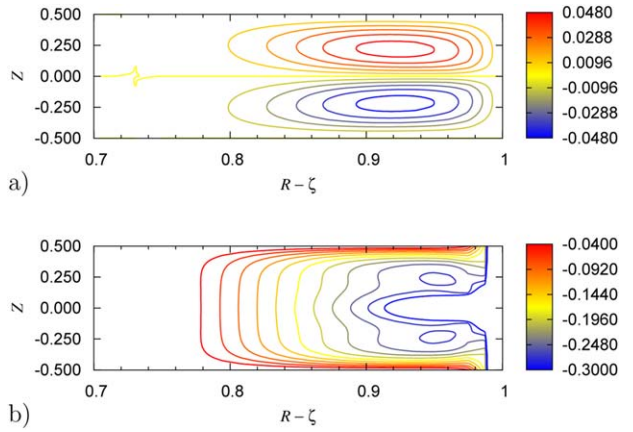

Figure 2. Velocity field obtained for $Re = 13710$, $S = 0.197$, and $\eta = 0.537$.

(a) Flow streamlines with Ψ levels ranging between -0.0480 and 0.0480 with an increment of 0.00962. Note that since the Ψ-scaling used in Ref. 21 was $\Omega HR_2^2(1-\eta^2)/2$ instead of the current ΩHR_2^2, the calculated streamfunction values were multiplied by a factor of 2.81 to facilitate comparison. (b) Contours of V levels ranging between -0.300 and -0.040 with an increment of 0.026. [Color figure can be viewed in the online issue, which is available at wileyonlinelibrary.com.]

can imagine that in real operation, there would be a short time interval between the instant when the solution is poured into the reactor and the moment when the disks begin to rotate. During such an interval, when we have $Re = 0$, a very small amount of reactant will be already consumed. Following the same approach as in Ref. 5, a 1-D solution, $\hat{C}(\tau, Z)$, of 14–16 in the limiting no-convection case ($Re = 0$) at a very short integration time ($\tau_0 = 0.001$) is extended radially to obtain the 2-D field $C(0, R, Z)$.

In each particular run, the system 26 was advanced in time until the target reactant conversion, $\chi(\tau = \tau_{90}) = 0.90$, was reached. Note that the volume-averaged reactant concentration will always decrease with time, and therefore, the reactant conversion $\chi(\tau)$ will be continuously growing. As it is shown below, one of the goals of this study is the prediction of the final operation time τ_{90}. The system 26 was advanced in time by means of a BDF2 scheme,[29] which is a second-order implicit method

$$\hat{\mathbf{B}}\left(\frac{3\mathbf{c}^{n+1}-4\mathbf{c}^{n}+\mathbf{c}^{n-1}}{2\Delta\tau}\right)=\hat{\mathbf{L}}\mathbf{c}^{n+1}+\hat{\mathbf{A}} \tag{27}$$

At each time step, the linear system 27 was solved for the values of the expansion coefficients at the new time step, $\mathbf{c}^{n+1}$, using the LAPACK numerical package.[30,31] The BDF2 scheme has the property of being unconditionally stable, that is, the error in the integration of 27 remains bounded for any $\Delta\tau > 0$. Notwithstanding, the time step had to be kept small enough to guarantee that the relative errors in both τ_{90} and in the corresponding efficiency value, $\eta(\tau_{90})$, were not larger than 10^{-3}. A value of $\Delta\tau = 10^{-5}$ was found to meet the above criterion in all of the cases investigated.

Accuracy Assessment

Since the flow between a pair of corotating disks has been thoroughly investigated in the last decades the accuracy of the current numerical results can be checked by comparing them with some well-established numerical results. In particular, we compared our results with those obtained by Ref. 21 for $Re = 13{,}710$, $S = 0.091$, and $\gamma = 0.537$. Figures 2a, b, respectively, show the current calculated contours of Ψ and V that were obtained with $N_{R,\Psi} = N_{Z,\Psi} = 21$. These results are in agreement with the corresponding contours reported in Figure 2 of Ref. 21, where a second-order finite difference method with grid sizes as large as 200 and 100 in the radial and axial directions, respectively, was used instead. Since $\zeta = 0$ was assumed in Ref. 21, the modified radial coordinate $R-\zeta$ was used in Figure 2 to facilitate comparisons. Note that in this study, the dimensionless radial distance from the outer enclosure wall is not $1-R$ but $1+\zeta-R$.

Thus, the use of the approximated velocity profile 24 at the disk surfaces with the current $\zeta = 0.05$ does not significantly alter the calculated velocity fields with respect to the basic $\zeta = 0$ case. To further assess, the effect of the ζ value on the present results, Figure 3a compares the evolution in time of the reactor efficiency, $\eta(\tau)$, for the two values

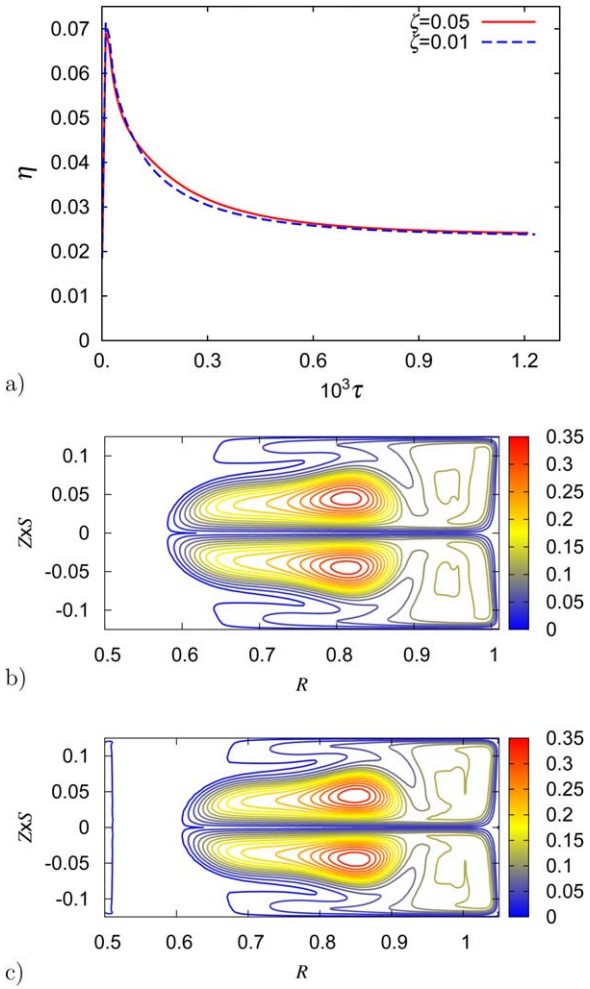

Figure 3. Assessment of the effect of the dimensionless radial gap, ζ for the case with $S = 0.25$, $Re = 7\times10^4$, $Sc = 100$, and $\phi = 2000$.

The evolution in time of the reactor efficiency, η, is compared in (a) for two calculations with $\zeta = 0.01$ and 0.05, respectively. The corresponding concentration contours at the target time $\tau = \tau_{90}$ are, respectively, plotted in (b) and (c). [Color figure can be viewed in the online issue, which is available at wileyonlinelibrary.com.]

Table 1. Maximum and Average Errors, Respectively, Denoted as Ek and $\bar{E}_{kj}$ for the Case with S = 0.25, $Re=10^4$, Sc = 10, $\phi=20$, and $\Delta N=6$

N_k-N_{k-1}	E_k	E_{kj}
47 − 41	1.32×10^{-3}	5.14×10^{-4}
53 − 47	8.55×10^{-4}	1.48×10^{-4}
59 − 53	4.21×10^{-4}	1.28×10^{-4}
65 − 59	3.43×10^{-4}	8.30×10^{-5}
71 − 65	8.47×10^{-5}	2.48×10^{-5}

$\zeta=0.01$ and $\zeta=0.05$ when the rest of parameters are fixed to $S=0.25$, $Re=7\times10^4$, $Sc=100$, and $\phi=2000$. The difference between the two $\eta(\tau)$ curves is small during the whole integration time. Moreover, Figures 3b, c, respectively, show the corresponding concentration fields obtained at an integration time $\tau=\tau_{90}=2.2\times10^{-3}$. The concentration contour lines in both plots are very similar, with only a slight difference in the radial region nearest to the outer enclosure wall, $R\approx1$.

Although values of the truncation parameters as small as $N_{R,\Psi}=N_{Z,\Psi}=21$ provided enough accuracy in the test results of Figure 2, a minimum of $N_{R,\Psi}=41$ and $N_{Z,\Psi}=41$ were used in the present calculations even for the smaller Reynolds numbers considered, $Re=10^3$. For the particular $S=0.25$ value, at which calculations were extended up to a higher Reynolds number of $Re=10^5$, the number of basis functions in expansions 22 and 23 had to be increased with increasing Re up to $N_{R,\Psi}=N_{Z,\Psi}=91$. Calculations with $Re\le2\times10^4$ and $S\ge0.5$ also required an increase in the truncation parameter $N_{Z,\Psi}$ up to a maximum value of $N_{Z,\Psi}=101$ for $S=1$ and $Re=2\times10^4$. The accuracy of velocity calculations was evaluated following the same procedure that is explained below for the concentration field except that the control quantity used was the radially averaged radial component of velocity, $\hat{U}$, instead of $\hat{C}$.

The selection of appropriate values of the truncation parameters to solve the mass-transfer problem 14–16, N_R and N_Z in expansion 25, was much more involved because of the effect of the Schmidt number on numerical accuracy. Even though the solutions of Eqs. 27 yield a spectral representation of the concentration field, that is, the values of the c_{ij} coefficients in expansion 25, it seems more natural to assess numerical accuracy at the physical level. This was achieved by computing the axial profiles of the radially averaged concentration, $\hat{C}(\tau,Z)$, on a uniformly spaced grid with 501 points along the Z direction. A preliminary set of calculations (which will be denoted hereinafter by the $k=0$ index) was performed using the same values of the truncation parameters in expansion 25 that were previously used in the corresponding velocity calculation, namely $N_R=N_{R,\Psi}$ and $N_Z=N_{Z,\Psi}$. Both N_R and N_Z were then equally increased by a fixed value ΔN to obtain a second set ($k=1$) of results, which were compared to the previous ones with lower resolution ($k=0$). In those cases where the convergence criterion was not fulfilled subsequent refinements ($k=2, 3,\ldots$) were applied. Let E_k, defined as

$$E_k=\max_{j=1,\ldots,501}E_{kj}=\max_{j=1,\ldots,501}\left\{\left|\frac{\hat{C}_k(\tau_{90},z_j)-\hat{C}_{k-1}(\tau_{90},z_j)}{\hat{C}_k(\tau_{90},z_j)}\right|\right\}, \tag{28}$$

denote the relative difference between two axial profiles calculated at refinement levels $k-1$ and k. The convergence criterion in all cases was set to $E_k/\Delta N\le10^{-4}$, that is, in terms of the slope of the E vs. N curve. Table 1 illustrates the convergence process for a calculation with $S=0.25$, $Re=10^4$, $Sc=10$, and $\phi=20$. In this particular case, a refinement level up to $k=5$ was necessary as a rather small $\Delta N=6$ was prescribed. Note that the accuracy of the $\hat{C}(\tau_{90},Z)$ profiles also depends on the accuracy of the predicted τ_{90} values in each calculation. The (N_R, N_Z) values of the converged solution increased with increasing Re and Sc. As expected, the problem parameter that mostly affected the accuracy of results was the Schmidt number. For $Sc=1$, only a few cases required a refinement level $k>1$. Values of the truncation parameter $N=\max(N_R,N_Z)$ up to $N=211$ had to be used in the calculations with $Sc=100$ as illustrated in Table 2 for the case with $S=0.25$, $Re=8\times10^4$, $Sc=100$, and $\phi=2000$. Note that in this case, numerical convergence is achieved for a $k=4$ refinement level but a much higher $\Delta N=30$ was used to cope with the effects of the higher Schmidt number. Not surprisingly, the most demanding calculations were those for $Sc=1000$ where values as large as $N=265$ had to be used in some cases.

Results and Discussion

In this work, four different values of the Schmidt number, namely $Sc=1$,10,100 and 1000, and several values of the Damköhler number within the range $1\le\phi\le8000$ were considered. Note that values of $Sc\approx1$ would typically be found in a gas-phase reactor at atmospheric pressure while the largest $Sc=1000$ value is typical of a liquid-phase reactor. For each particular (Sc, ϕ) pair, calculations were performed at several values of Re and S, as is explained in what follows. A unique value of the radius ratio, $\gamma=0.5$, was used in all of the present calculations.

Velocity field

Velocity fields were calculated at four different values of the height to radius aspect ratio, namely $S=0.125$, 0.25, 0.50, and 1, and four different values of the Reynolds number, namely $Re\times10^{-3}=1$, 5, 10 and 20. In addition, for the particular $S=0.25$ value, calculations were extended up to a Reynolds number of $Re=10^5$. Figure 4 shows the flow streamlines (isolines of the streamfunction Ψ) calculated at $Re=2\times10^4$ and two different aspect ratios, $S=0.125$ and 0.25. Note that the velocity fields plotted in these two figures are symmetric with respect to the horizontal midplane ($Z=0$). Although this feature may seem quite natural, the existence of solution branches with symmetry-breaking has also been reported.[19,21,23] The present numerical method allows the calculation of such symmetry-breaking solutions, as both even and odd functions along the Z direction were used in expansions 22 and 23. Notwithstanding, only symmetric solutions were detected in all of the cases investigated. As a consequence, only Chebyshev polynomials of even degree were considered along the Z direction in the

Table 2. Maximum and Average Errors, Respectively, Denoted as Ek and $\bar{E}_{kj}$ for the Case with S = 0.25, $Re=8\times10^4$, Sc = 100, $\phi=2000$, and $\Delta N=30$

N_k-N_{k-1}	E_k	$\bar{E}_{kj}$
121 − 91	9.35×10^{-4}	3.73×10^{-4}
151 − 121	3.11×10^{-4}	1.96×10^{-5}
181 − 151	1.02×10^{-4}	9.69×10^{-6}
211 − 181	5.11×10^{-5}	6.73×10^{-6}

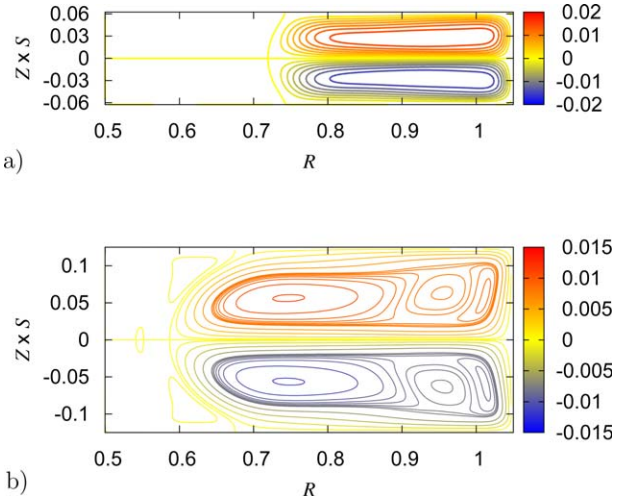

Figure 4. Flow streamlines calculated for $Re=2\times10^4$ and both $S=0.125$ (a) and $S=0.25$ (b).

[Color figure can be viewed in the online issue, which is available at wileyonlinelibrary.com.]

concentration expansion 25. Therefore, $\hat{C}$ and η in 17 can be indistinctly calculated either at $Z=-1/2$ or $Z=1/2$.

Figure 4 shows the cross-stream motion that is typical of the flow between a pair of corotating disks. In the vicinity of both disk surfaces, fluid is moving outward along the boundary layer region known as Ekman layer. It should be kept in mind that, as illustrated in Figure 2b, the main motion occurs in the circumferential direction, that is, it would be normal to the paper in Figure 4. The secondary motion is basically driven by the imbalance between the inward directed radial pressure force and the outward directed centrifugal force along the disk Ekman layers (see, e.g., the theoretical analysis in Ref. 17 and the references therein). Moreover, as shown in Figure 2b, the radial region around $R=1$ is characterized by very high shear levels as the circumferential velocity, V, must drop to its minimum $V=-1$ value at the outer enclosure wall.

As can be seen in Figures 2 and 4, when the aspect ratio S is small the cross-stream vortices do not reach the vicinity of the rotating hub as there is an inner core region where fluid is nearly in solid-body rotation with the disks and hub, that is, $V\approx0$, with cross-stream motion much weaker than the one in the outer region. Let $R_{sep}=R_{sep}(Re,S)$ be the radial location where the separation between the Ekman layer region and the inner core is observed at the disk surface. In the case with $S=0.125$, which is the most unfavorable in terms of effective catalyst surface, we have $R_{sep}=0.73$ in Figure 4a, and therefore, the Ekman layer region ($R>R_{sep}$) extends over about 2/3 of the total disk surface. The R_{sep} location decreases with increasing S down to the point that at $S=1$, there is no inner core.

According to theory, the thickness of the Ekman layer, $\delta_E\propto\sqrt{\nu/\Omega}$, and thus

$$\delta_E/H\propto Re^{-1/2}S^{-1} \tag{29}$$

For each of the present calculations, a radially averaged value of the Ekman layer thickness, $\hat{\delta}_E$, was estimated as follows. We first averaged the radial component of velocity, $U(R,Z)$, within the radial region with $R_{sep}\le R\le1$ to obtain the axial profiles $\hat{U}(Z)$. Figure 5 shows the $\hat{U}(Z)$ profiles for two different aspect ratios, $S=0.125$ and 0.50. In almost all of the cases, $\hat{U}$ raises quickly from the zero value at the disk surface up to a maximum value and then it drops down to a negative minimum value at the $Z=0$ midplane (where the strongest inward cross-stream flow is observed in Figure 4). A straightforward estimate of $\hat{\delta}_E/H$ is, therefore, obtained by measuring the axial distance between the location of the maximum and the nearest disk surface. The anomalous profile at $Re=1000$ in Figure 5a is due to the fact that at such low Re value the Ekman layer is not well developed yet. A least squares fit of the estimated $\hat{\delta}_E/H$ values yielded

$$\frac{\hat{\delta}_E}{H}=1.12\,S^{-1.020}Re^{-0.517} \tag{30}$$

thus, in qualitative agreement with the scaling suggested by theory. The anomalous data point at $Re=1000$ and $S=0.125$ was not included in the fit.

Influence of the height to radius aspect ratio

In this section, the performance of the reactor is assessed as a function of the height to radius aspect ratio, S. In practice, one would have a setup with a fixed R_2 value and the question would be what value of the height H should be

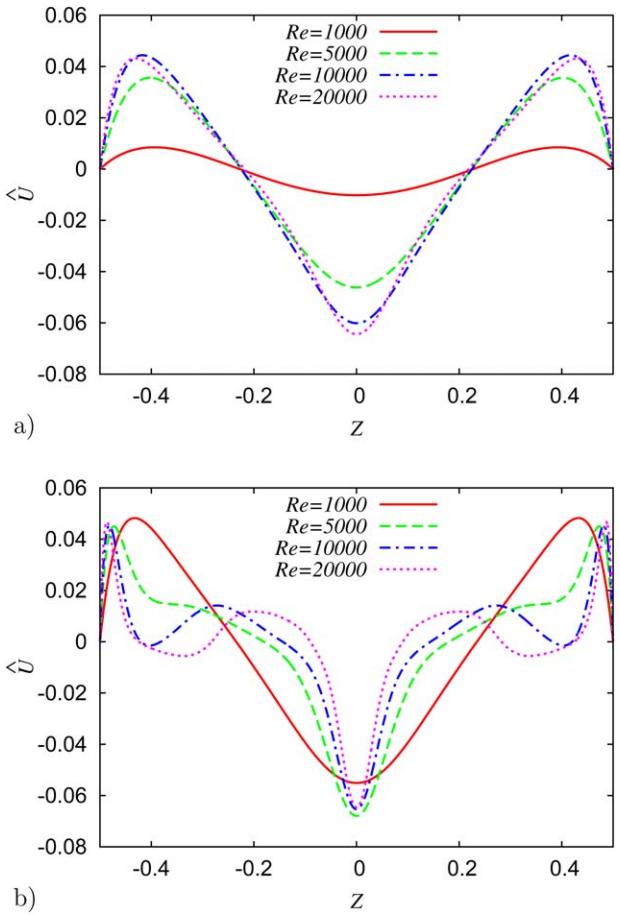

Figure 5. Axial profiles of the radially averaged radial component of velocity, $\hat{U}(Z)$, for four different values of the Reynolds number in the range $10^3\le Re\le2\times10^4$ and both $S=0.125$ (a) and $S=0$. (b).

[Color figure can be viewed in the online issue, which is available at wileyonlinelibrary.com.]

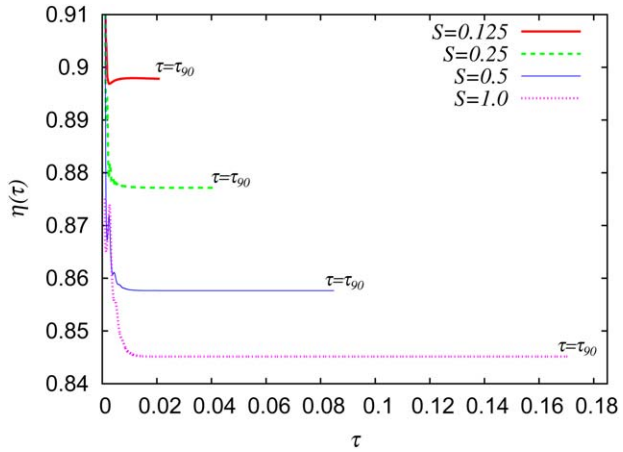

Figure 6. Evolution in time of the reactor efficiency, $\eta(\tau)$, for $Re=1\times10^4$, $Sc=1$, $\phi_0=1$, and all of the four values of S investigated.

[Color figure can be viewed in the online issue, which is available at wileyonlinelibrary.com.]

chosen. Note that for a single disk pair a given reactor volume would be achieved by modifying H alone but if a larger number of disks are allowed there is also the option to add more disks to the stack. The second option would require a larger investment but it is obviously preferable in terms of mass-transfer efficiency because a higher ratio of surface catalyst to reactor volume, $a_g=2/H$, would be maintained.

Four different values of the height to radius aspect ratio, namely $S=0.125$, 0.25, 0.5, and 1.0, and four values of the Reynolds number, $Re\times10^3=1, 5, 10$, and 20 were considered. Once the velocity fields were obtained for each of the 16 (Re, S) pairs, four values of Sc and four values of ϕ were considered in each case, thus, giving a total of 256 calculations. Since the Damköhler number, $\phi=kH/D$, is defined on the basis of H, the value of ϕ must be changed along with the value of S to assess the effect of an increase in H alone. That is, if at $S=0.125$, we set a given $\phi=\phi_0$ value then at the corresponding calculation at $S=0.25$, we set $\phi=2\phi_0$, and so on.

Figure 6 shows the evolution in time of the reactor efficiency, η, for all of the four values of S investigated when the rest of parameters are fixed to $Re=10^4$, $Sc=1$, and $\phi_0=1$. As expected, the time τ_{90} needed to achieve the target reactant conversion clearly increases with increasing S. It is remarkable that after a relatively short transient $\eta(\tau)$ reaches a plateau-like, constant value. Such a behavior in the time evolution of η was also previously observed for the natural convection-driven cubical reactor in Ref. 5. In all of the present calculations, $\eta(\tau)$ achieves a maximum value during the transient and then experiences a considerable drop until it reaches the final asymptotic value. Such an asymptotic value of the reactor efficiency will be hereinafter denoted by η_∞ and τ_∞ will denote the smallest dimensionless time fulfilling $\eta(\tau\geq\tau_\infty)=\eta_\infty$.

The asymptotic time evolution of the reactor efficiency is due to the fact that the quantity

$$\Sigma(\tau,R,Z)=\frac{C(\tau,R,Z)}{\bar{C}(\tau)} \tag{31}$$

becomes independent of time for $\tau\geq\tau_\infty$, that is, we can define $\Sigma_\infty(R,Z)=\Sigma(\tau,R,Z):\tau\geq\tau_\infty$. Figures 7 and 8, respectively, show the contours of $\Sigma_\infty(R,Z)$ obtained for $S=0.125$ and $S=0.25$ at $Re=2\times10^4$, three different values of the Schmidt number, namely $Sc=1$, 10, and 1000, and two values of ϕ_0. When the reaction is comparatively fast, $\phi_0=100$ in plots (b), (d), and (f) of both figures, $\Sigma_\infty(R,\pm1/2)\rightarrow0$ which

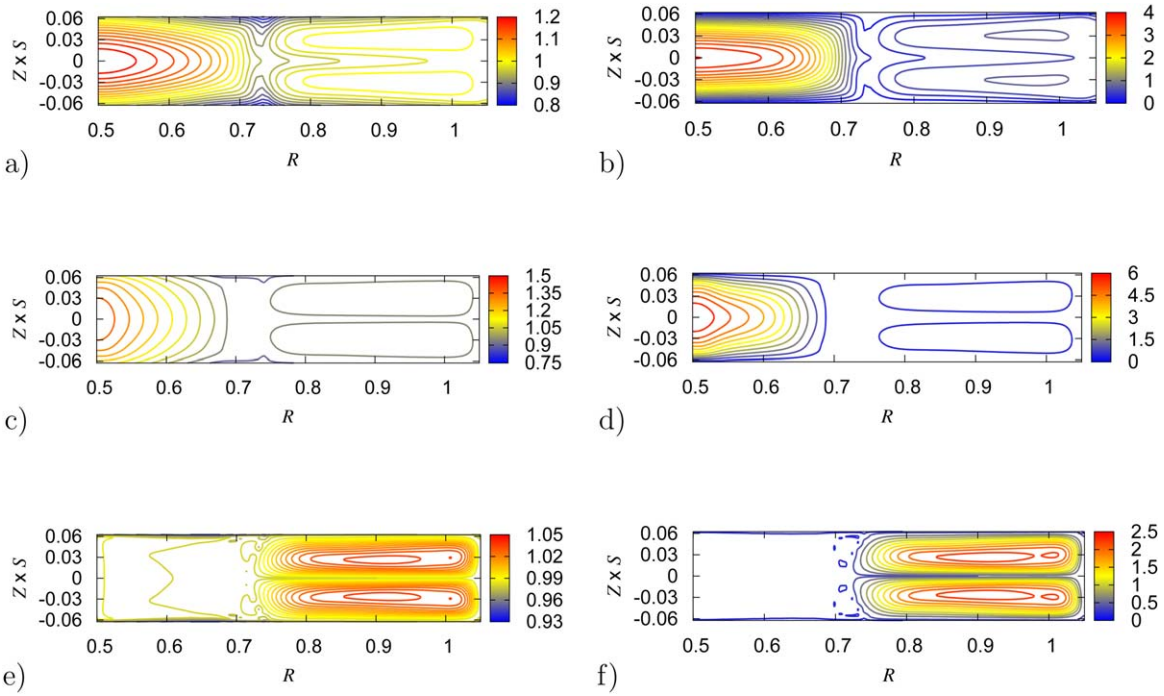

Figure 7. Contours of the normalized concentration, Σ_∞, for $S=0.125$ and $Re=2\times10^4$.

The values of the Damköhler number are $\phi=1$ in plots (a), (c), and (e) and $\phi=100$ in plots (b), (d), and (f). The values of the Schmidt number are $Sc=1$ in plots (a) and (b), $Sc=10$ in plots (c) and (d) and $Sc=1000$ in plots (e) and (f). [Color figure can be viewed in the online issue, which is available at wileyonlinelibrary.com.]

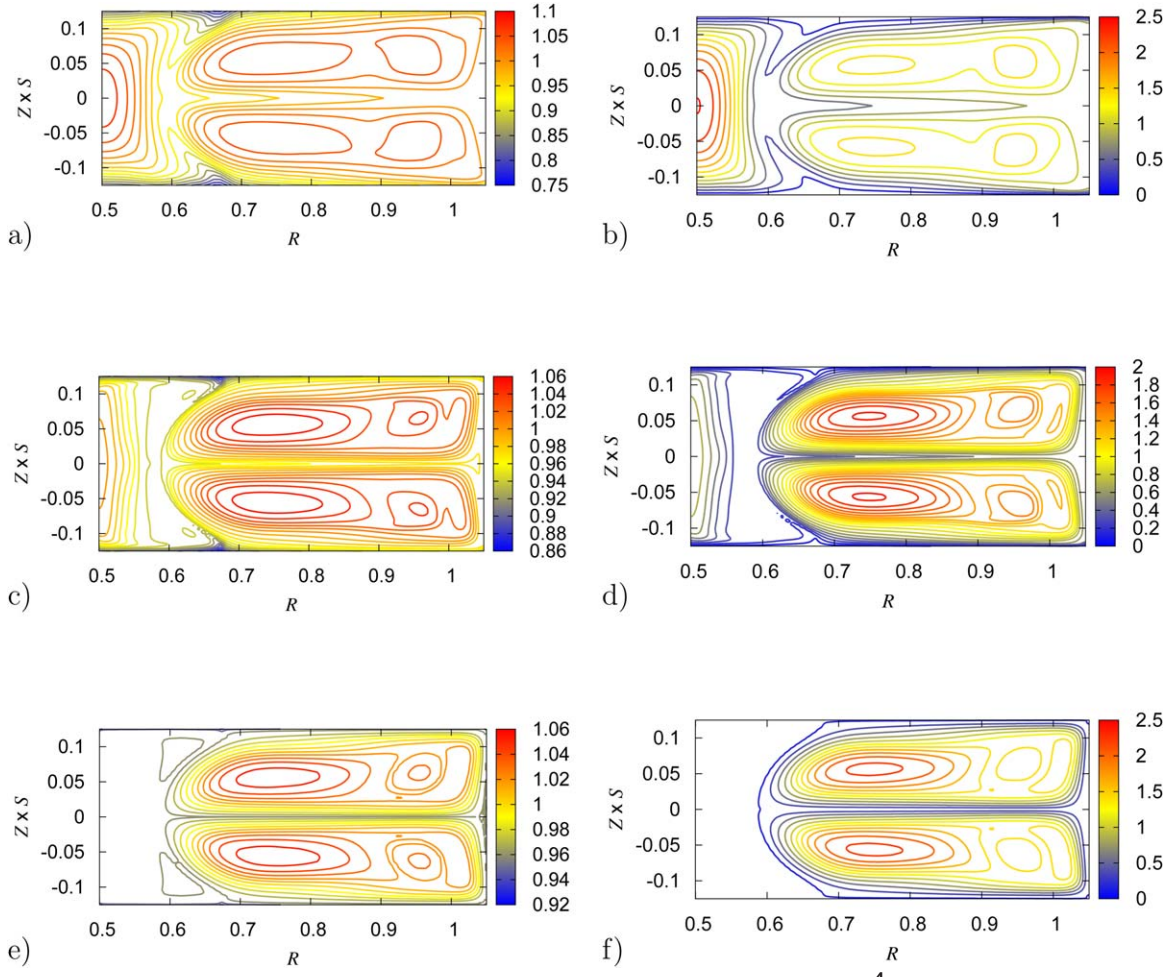

Figure 8. Contours of the normalized concentration, Σ_∞, for $S = 0.25$ and $Re = 2\times10^4$.

The values of the Damköhler number are ϕ=2 in plots (a), (c), and (e) and ϕ=200 in plots (b), (d), and (f). The values of the Schmidt number are $Sc = 1$ in plots (a) and (b), $Sc = 10$ in plots (c) and (d) and $Sc = 1000$ in plots (e) and (f). [Color figure can be viewed in the online issue, which is available at wileyonlinelibrary.com.]

means, on account of 17, that the reactor efficiency will be small. The maximum Σ_∞ values are much higher in all of the cases with $\phi_0 = 100$ than in the corresponding cases with $\phi_0 = 1$. At $Sc = 1$, plots (a) and (b) in Figures 7 and 8, the largest Σ_∞ levels are observed within the inner core, $R < R_{sep}$. Thus, for the case with faster molecular diffusion ($Sc = 1$), the maximum resistance to mass transfer is a consequence of the weakness of the convective transport within the inner core. On the contrary, in the concentration contours for $Sc = 1000$, plots (e) and (f), the maximum Σ_∞ values are found in the center of the cross-stream vortices. That is, when resistance to mass transfer is mostly due to molecular diffusion some reactant remains trapped within the vortices and it cannot easily reach the Ekman layers.

As will be seen in the next subsection, according to theory, the Sherwood number, Sh_∞, should be independent of S. Then, since in this section, we are considering constant values of the ϕ/S ratio it follows from (20) that for a given ϕ_0 value η_∞ should be also independent of S. Present results with $Sc = 1$ are in fairly good agreement with the expected theoretical behavior, as illustrated in Figure 6, for the case with $Re = 10^4$, $Sc = 1$, and $\phi_0 = 1$, in which the maximum variation of η_∞ with S is within 6%. However, as it is shown in Figure 9, departures from theory become increasingly significant with increasing values of ϕ_0 and, especially, of Sc. This figure shows time evolutions of $\eta(\tau)$ for all the four values of S when the rest of parameters take the value $Re = 2\times10^4$, $Sc = 1000$, and $\phi_0 = 100$. Note that as a

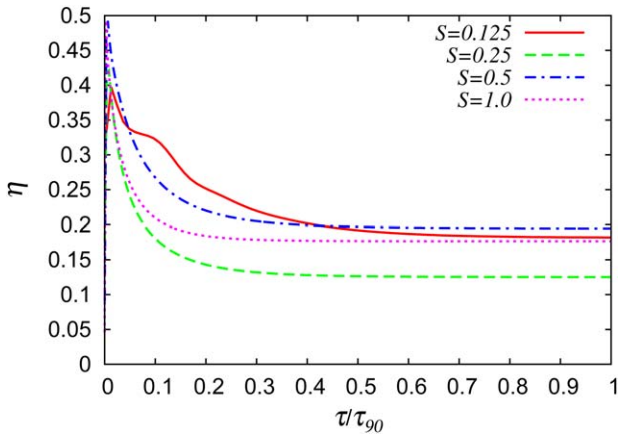

Figure 9. Evolution in time of the reactor efficiency, $\eta(\tau)$, for $Re = 2\times10^4$, $Sc = 1000$, $\phi_0 = 100$, and all of the four values of S investigated.

[Color figure can be viewed in the online issue, which is available at wileyonlinelibrary.com.]

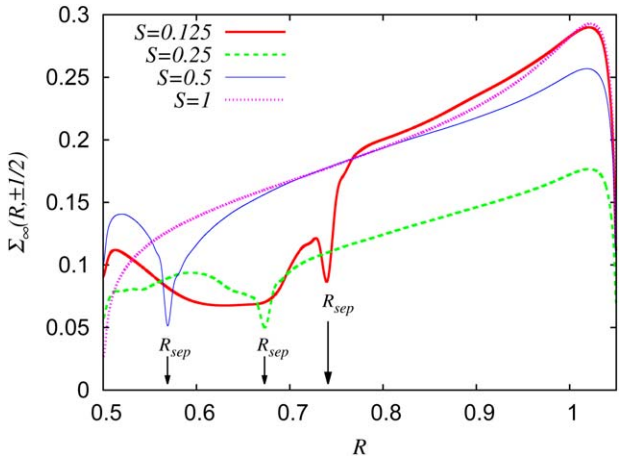

Figure 10. Radial profiles of the normalized concentration at the disk surface, $\Sigma_\infty(R,\pm1/2)$, for $Re=2\times10^4$, $Sc=1000$, $\phi_0=100$, and all of the four values of S investigated.

[Color figure can be viewed in the online issue, which is available at wileyonlinelibrary.com.]

consequence of the high value of ϕ_0 used in these calculations, the initial transients are not negligible, that is, $\tau_\infty/\tau_{90} \gg 0$. Moreover, Figure 9 shows that, whereas the η_∞ values for $S=0.125, 0.5$, and 1 are around 0.18, the corresponding value for $S=0.25$ is anomalously smaller by about a 30%.

Figure 10 shows the radial profiles of $\Sigma_\infty(R,\pm1/2)$ for the case with $Re=2\times10^4$, $Sc=1000$, and $\phi_0=100$ (i.e., the same conditions as in Figure 9) and all of the four values of S. In all of the profiles, the maximum Σ_∞ value is attained near the enclosure wall, $R\approx1.02$, roughly at the location where the cross-stream vortices detach from the disk surface. In the case with $S=0.25$, the maximum value, $\Sigma(1.02,\pm1/2)=0.18$, is considerably lower and this deficit is maintained in the whole region with $R\geq R_{sep}$. The lower η_∞ value for $S=0.25$ in Figure 9 is to be, therefore, attributed to the lower ability of the cross-stream flow to transport reactant from the bulk region into the vicinity of the disk surface at this particular aspect ratio. We can also see in this Figure 10 that on the average the $\Sigma(R,\pm1/2)$ levels are smaller but not negligible in the inner core, $R\leq R_{sep}$. Thus, inspection of Figures 9 and 10 together suggest the relative size of the inner core has only a slight effect on η_∞.

Analysis of mass-transfer efficiency

Our main purpose here is to correlate the mass-transfer efficiency as a function of the problem parameters, Re, Sc, ϕ, and S. In addition, we aim to understand better to what extent the overall mass-transfer rates are boundary layer controlled or, as was shown in the previous subsection, other sources of resistance to mass transfer may also play a relevant role. At a qualitative level, it is observed that all of the calculated η_∞ values increase with increasing Re and Sc and decrease with increasing ϕ. To better capture the Reynolds number dependence, additional calculations were performed for $S=0.25$ and Reynolds numbers between $Re=4\times10^4$ and 10^5 every 10^4 units.

If the transport of reactant into the disk surface is to be controlled by the rate of molecular diffusion within the disk boundary layer then one would expect a dependence for the Sherwood number of the form $Sh\propto Re^{1/2}Sc^{1/3}$.[32] Note that this scaling for Sh is consistent with the theoretical dependence for the concentration boundary layer thickness, δ_C, on the Schmidt number, that is, $(\delta_C/\delta_E)\propto Sc^{-1/3}$, because $\delta_E/R_2\propto Re^{-1/2}$ (Eq. 29). Or in other words, the Sherwood number would theoretically scale with δ_C according to $Sh\propto R_2/\delta_C$. In our previous work on the natural convection-driven reactor in a cubical cavity,[5] a value of δ_C/H was estimated for each particular calculation and then a very good correlation for δ_C/H as a function of the Rayleigh and Schmidt numbers was obtained. Thus, in the problem investigated in Ref. 5, the overall mass-transfer rate was indeed boundary layer-controlled.

In this problem, however, it was not possible to obtain a reasonably accurate fit for δ_C/R_2. Furthermore, a direct fit for the Sherwood number yielded

$$\widetilde{Sh}(\tau_\infty)=\widetilde{Sh}_\infty=1.98S^{-0.0792}Re^{0.373}Sc^{0.137}\phi^{-0.0347} \qquad (32)$$

Figure 11a shows that this fit did neither produce an accurate correlation, with a relative root mean square error as

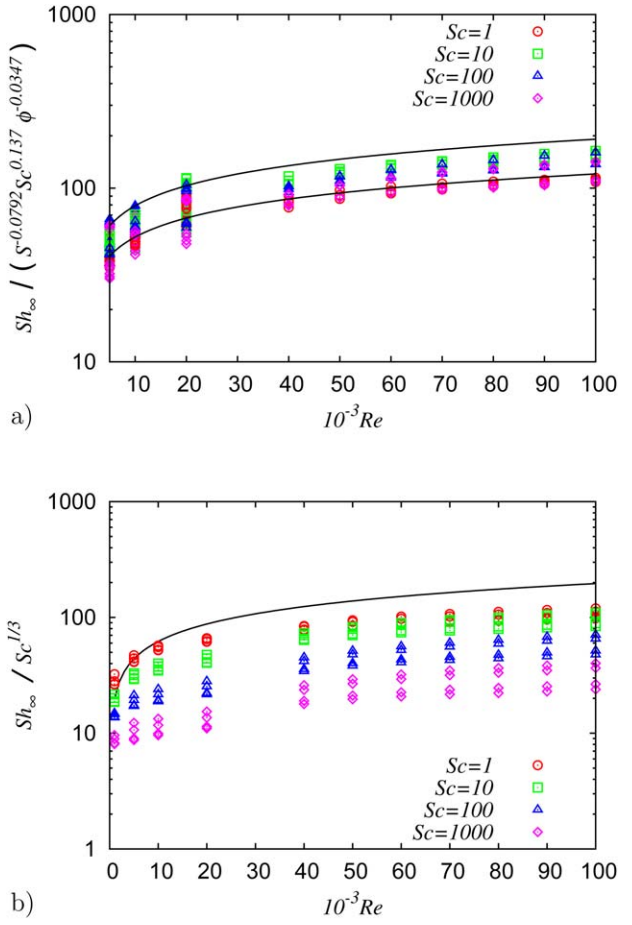

Figure 11. Variation with Re of the predicted values of the Sherwood number, Sh_∞, for all of the current calculations.

In (a), Sh_∞ is divided by $S^{-0.0792}Sc^{0.137}\phi^{-0.0347}$; the two solid lines denote the boundaries of the 95% confidence interval for the fit. In (b), Sh_∞ is divided by $Sc^{1/3}$ instead and the theoretical boundary-layer prediction, Eq. 33, is plotted with a solid line. In both plots, circles, squares, triangles, and diamonds, respectively, denote the results obtained with $Sc=1$, 10, 100, and 1000. [Color figure can be viewed in the online issue, which is available at wileyonlinelibrary.com.]

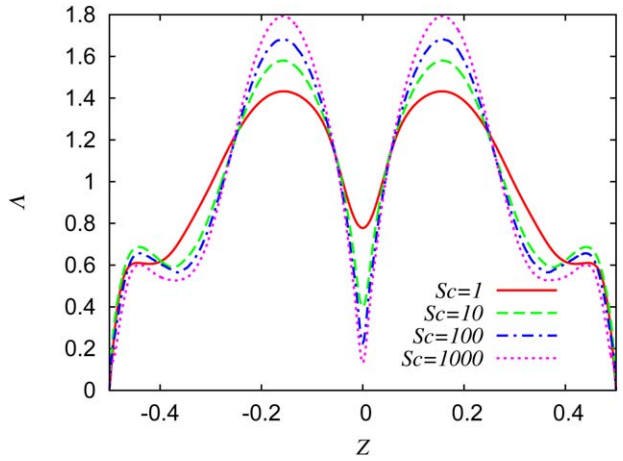

Figure 12. Axial profiles of the radially averaged normalized concentration, $\Lambda(Z)$ defined by Eq. 34, for $Re=6\times10^4$, $\phi=2000$, $S=0.25$, and all of the four values of the Schmidt number investigated.

[Color figure can be viewed in the online issue, which is available at wileyonlinelibrary.com.]

large as 0.183. The fit 32 shows, as expected, a very small dependence of mass-transfer efficiency on the Damköhler number ϕ. In addition, since the characteristic length R_2 was used to define Sh, the influence of S on Sh is also small. The comparison of present results with the theoretical dependence[32]

$$Sh=0.62Re^{1/2}Sc^{1/3} \tag{33}$$

shown in Figure 11b, reveals that mass-transfer efficiency in the present problem is lower than it would be for the laminar boundary layer flow over a freely rotating disk. Note that the exponent of Sc in the fit 32 is anomalously below the theoretical 1/3 value so that the lower efficiency of the current setup gets increasingly evident in Figure 11b as the Schmidt number increases.

Our hypothesis is that in the current problem, the overall mass-transfer process is not, in general, boundary layer-controlled. To obtain further support for such a hypothesis, we examined the distribution of the radially averaged normalized concentration

$$\Lambda(Z)=\frac{\hat{C}(\tau_\infty,Z)-\hat{C}(\tau_\infty,-1/2)}{\bar{C}(\tau_\infty)-\hat{C}(\tau_\infty,-1/2)}=\frac{\hat{\Sigma}_\infty(Z)-\eta_\infty}{1-\eta_\infty}. \tag{34}$$

Figure 12 shows the axial profiles of Λ for the cases with $S=0.25$, $Re=6\times10^4$, and $\phi=2000$, and all of the four values investigated of the Schmidt number, $Sc=1$, 10, 100, and 1000. In all of the cases, the $\Lambda(Z)$ profile has a local maximum of about $\Lambda=0.6-0.7$ not far from the disk surface ($|Z|>0.4$). Note that if Fick's law is applied to the radially averaged concentration field, the presence of such a local maxima of Λ suggests that, on the average, molecular diffusion along the Z-direction is not transporting reactant from the bulk region into the disk boundary layers. In all of the four profiles of Figure 12, the global maxima are located in the bulk region, around $|Z|=0.17$. The maximum Λ value increases with increasing Sc. Since the corresponding values of Λ at the local minima at $Z=0$ decrease with increasing Sc instead it follows that the global concentration drop $\Delta\Lambda$ raises with Sc, from $\Delta\Lambda=0.6$ units at $Sc=1$ up to $\Delta\Lambda=1.7$ units at $Sc=1000$.

In summary, we see that as molecular diffusion becomes slower (larger Sc) an increasingly higher amount of solute accumulates in the bulk region, an indication that the overall resistance to mass transfer has increased. Since direct transport by molecular diffusion into the disk boundary layer does not seem to work reactant is instead diffused into the midplane region ($Z\approx0$), where fluid is returned radially inward (Figure 4), before it is eventually convected into the Ekman layer region.

Prediction of the target operation time

In this subsection, we will show how the predicted values of the reactor efficiency, η_∞, can be used to estimate the time needed to achieve a target reactant conversion. Following the methodology first implemented in Ref. 5, first, we integrate the differential molar balance equations 14–16 over the whole reactor volume

$$\frac{d\bar{C}(\tau)}{d\tau}=-\frac{2\phi}{S^2}\hat{C}(\tau,\pm1/2) \tag{35}$$

Then, we introduce the $\eta(\tau)$ definition 17 in the above equation to obtain

$$\frac{d\bar{C}(\tau)}{d\tau}=-\frac{2\phi\eta(\tau)}{S^2}\bar{C}(\tau) \tag{36}$$

The ODE 36 can be integrated using $(\tau_\infty,\bar{C}(\tau_\infty))$ as initial condition and assuming $\eta(\tau)=\eta_\infty$

$$\frac{\bar{C}(\tau)}{\bar{C}(\tau_\infty)}=\exp\left[\frac{-2\phi\eta_\infty}{S^2}(\tau-\tau_\infty)\right] \tag{37}$$

Assuming that the transient is short, that is, $\tau_\infty\to0$ and $\bar{C}(\tau_\infty)\approx\bar{C}(0)$, Eq. 37 can be simplified into

$$-\frac{\bar{C}(\tau)}{\bar{C}(0)}\approx-\exp\left(\frac{-2\phi\eta_\infty\tau}{S^2}\right) \tag{38}$$

Thus, the evolution in time of the reactor conversion, $\chi(\tau)$, can be approximated by

$$\chi(\tau)=\frac{\bar{C}(0)-\bar{C}(\tau)}{\bar{C}(0)}\approx1-\exp\left(\frac{-2\phi\eta_\infty\tau}{S^2}\right) \tag{39}$$

If we set, for example, a target reactant conversion $\chi(\tau_{90})=0.90$, the final operation time can be, therefore, estimated as

$$\tilde{\tau}_{90}=-\ln(0.10)\left(\frac{S^2}{2\phi\eta_\infty}\right) \tag{40}$$

or on account of Eqs. 19 and 21

$$\tilde{\tau}_{90}=-\ln(0.10)\left[\frac{S}{2Sh_\infty(1-\eta_\infty)}\right]=-\ln(0.10)\left(\frac{S}{2Sh_{OV\infty}}\right) \tag{41}$$

Figure 13 shows a comparison between the $\tilde{\tau}_{90}$ estimates and the τ_{90} values obtained in the calculations. In Figure 13a, the calculated values of η_∞ were introduced in Eq. 40 to obtain $\tilde{\tau}_{90}$, whereas the values plotted in Figure 13b were obtained from approximate reactor efficiencies given by Eq. 20 with the $\widetilde{Sh}_\infty$ values that were calculated using the fit 32. We can see in Figure 13a that Eq. 40 produces a good

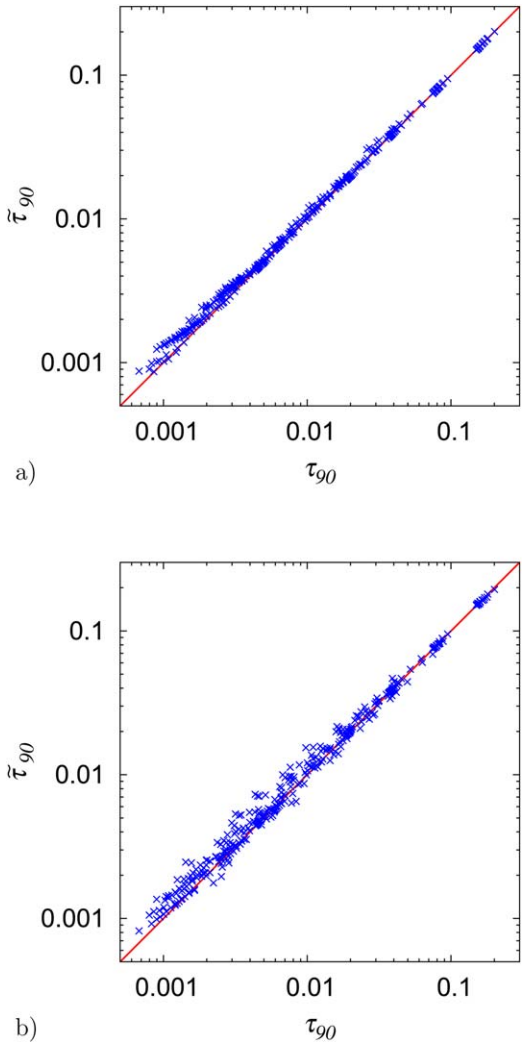

Figure 13. The values of τ_{90} predicted by Eq. 40, $\tilde{\tau}_{90}$, are plotted against the corresponding τ_{90} values obtained in all of the calculations.

In plot (a), the calculated η_∞ values were introduced into Eq. 40, whereas in plot (b), the estimated η values obtained from the fit 32 were used instead. [Color figure can be viewed in the online issue, which is available at wileyonlinelibrary.com.]

estimate of τ_{90}. The largest departures observed in this figure correspond to the smallest reaction times (small S and/or large ϕ values), that is, when $\tau_\infty/\tau_{90} \gg 0$ and the approximation 38 differs from the exact solution 37. Note that in such cases the predictions given by 40 are conservative, that is, the $\tilde{\tau}_{90}$ values overestimate the calculated τ_{90} because reactor efficiencies are higher than η_∞ during the initial transient. It is interesting that even the less accurate $\tilde{\tau}_{90}$ estimates based in the fit 32 show a reasonable agreement with the calculated τ_{90} in Figure 13b. In this respect, it is worth noting that the use of Eq. 40 together with Eq. 20 somehow masks part of the error in the Sh_∞ fit 32 as the relative root mean square error in terms of η_∞ and τ_{90} reduces to 0.134. Thus, it would not be necessary to perform a costly calculation to obtain a fast and fairly accurate prediction of the final operation time for the present discontinuous reactor.

Moreover, it seems also convenient to assess to what extent the current τ_{90} predictions are independent of the initial condition. As it was explained above, a nearly uniform distribution of reactant through the whole reactor volume is assumed as the initial condition for the O.D.E. system (26). Figure 14 compares, for the case with $S = 0.25$, $Re = 2\times10^4$, $Sc = 1$, and $\phi = 2$, the evolution in time of the reactant conversion obtained using this regular initial condition with the evolution obtained in a second calculation where the initial concentration distribution was arbitrarily set to $C(0,R,Z) = C_0 \exp\left[-(Z/0.1)^2\right]$ (here the value of C_0 is set so that $\bar{C}(0) = 1$). The two time evolutions are very similar, and we can see that the τ_{90} value obtained with the initial Gaussian axial profile is just about 0.2% higher than the τ_{90} obtained in the regular calculation. Since the number of disk revolutions per unit dimensionless time, τ, is equal to $ReSc/2\pi$, it takes about 129 disk revolutions to achieve the target 90% conversion for the conditions of Figure 14. As can be seen in the leftmost inset of Figure 14, the difference between the two calculations is established at very early integration times. The initial concentration distribution with a Gaussian axial profile implies the initial absence of reactant in the vicinity of the disks and it, therefore, produces a time evolution that is quite distinct from the regular one for a few disk spins. Another interesting side result, not apparent in Figure 14, is that both time integrations lead to respective distributions of the asymptotic normalized concentration, Σ_∞, that are identical within machine accuracy (and therefore the same applies to the respective values of η_∞). Some more thought will be given to this remarkable fact in the concluding remarks.

Mixing enhancement prospects

We have seen above that the mass-transfer efficiency in the current discontinuous reactor is hindered by low mixing levels as some reactant remains trapped in the region within the cross-stream vortices. In the rotor-stator reactor investigated by Meeuwse et al.,[11] these authors measured, for $Re = 10^5$, a value of Sh roughly in agreement with Eq. 33. Naturally, we wonder why our current setup should be less

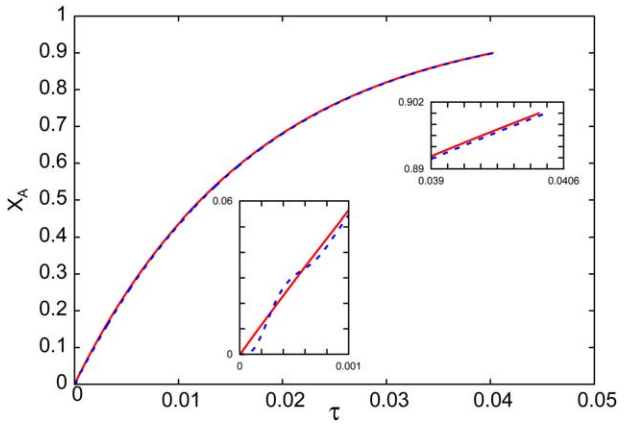

Figure 14. Evolution in time of the reactant conversion, X_A, for the case with $S = 0.25$, $Re = 2\times10^4$, $Sc = 1$, and $\phi = 2$.

The solid line corresponds to a calculation with the regular initial concentration distribution, whereas the dashed line shows the results of a second calculation initialized with a Gaussian distribution in Z, namely $C(0,R,Z) = C_0 \exp\left[-(Z/0.1)^2\right]$; here the value of the constant C_0 is set so that the initial value of the volume averaged concentration is exactly one. [Color figure can be viewed in the online issue, which is available at wileyonlinelibrary.com.]

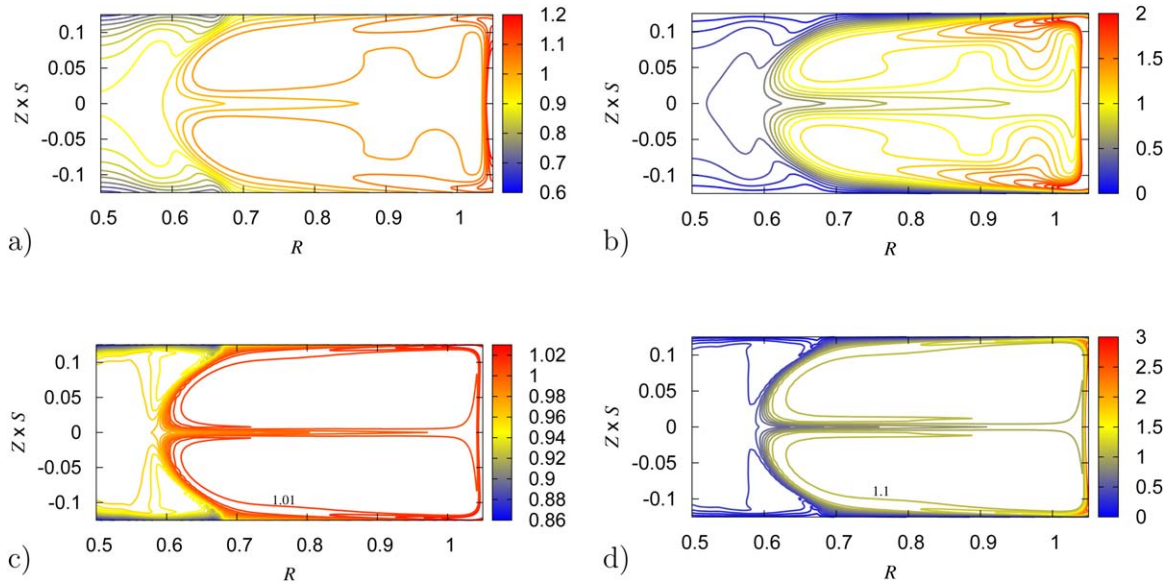

Figure 15. Concentration contours obtained with the modified reactor model for $S = 0.25$ and $Re = 2\times10^4$.

The values of the Schmidt number are $Sc = 1$ in plots (a) and (b) and $Sc = 10$ in (c) and (d). The values of the Damköhler number are $\phi = 2$ in plots (a) and (c) and $\phi = 200$ in (b) and (d). The quantity plotted in all four cases is the product $C_S(R,Z)\eta_S$, whose volumetric average is equal to one. [Color figure can be viewed in the online issue, which is available at wileyonlinelibrary.com.]

efficient than Meeuwse et al.'s. One plausible explanation is that Meeuwse et al.'s reactor operated in continuous mode with a stream of fresh reactant being fed through the radial gap between the edge of the rotating disk and the outer enclosure wall. Our purpose here is to explore a modified model of the current setup that, albeit not completely realistic, incorporates a continuous addition of reactant close to the external cylindrical wall. In particular, in the modified model the boundary condition for Eq. 14 at the outer enclosure wall is replaced by

$$\frac{\partial C}{\partial R} = J_R(Z) = -\beta \exp\left(Z^2/\sigma^2\right) \tag{42}$$

with $\sigma^2 = 0.1$. The Gaussian shape of the radial diffusion flux, $J_R(Z)$, in 42 was chosen because of it smoothness, that is, it avoids the incompatibility with Eq. 15 which, as discussed above, would be inherent to the choice of a flat axial profile for J_R. The value of β in 42 was calculated in each particular case by equating the total reactant consumption at the disk surfaces to the rate of reactant input through the enclosure wall and imposing the condition $\hat{C}(\tau, \pm 1/2) = 1$.

Calculations for the modified model were performed for the aspect ratio value of $S = 0.25$, two values of the Schmidt number, $Sc = 1$ and 10, and all of the Re and ϕ values that were previously considered for the original model. The discrete forms of Eqs. 14–16 with the modified boundary condition 42 were advanced in time starting from the initial condition $C(0,R,Z) = 0$. In all of the cases, a steady concentration field was reached after a relatively short transient, $\tau = \tau_S$. This steady concentration field, $C(\tau_S,R,Z) = C_S(R,Z)$, coincided with the one that was directly calculated by setting the time derivative term in 14 equal to zero. Contours of the quantity $C_S(R,Z)\eta(\tau_S)$, whose volumetric average is equal to $\bar{C}(\tau_S)\eta(\tau_S) = \hat{C}_S(\tau_S, \pm 1/2) = 1$, are shown in Figure 15. The highest concentration levels in Figure 15 are observed, not surprisingly, close to the external cylindrical wall. Since at $\tau = 0$, there is no reactant present within the inner core, the concentration levels in that region remain considerably lower than they were in the corresponding plots of Figure 8. Moreover, for $Sc = 10$, we see in Figure 15c, d that the concentration levels within the cross-stream vortices are only slightly above one. The corresponding maximum concentration levels (relative to the respective $\bar{C}(\tau_\infty)$ values) in Figure 8c ($\phi = 2$) and, especially, in Figure 8d ($\phi = 200$) were considerably higher. This means that in the modified model less reactant remains trapped in the bulk region. It is worth noting that we also tested a second modified reactor configuration with reactant being continuously fed through the inner hub ($R = \gamma$) instead. But with such an alternative feed, it was found that mixing was even poorer than it was the original discontinuous reactor as a large amount of reactant remained trapped in the inner core, $R \le R_{sep}$.

Figure 16 shows the axial profiles of Λ_S, calculated by replacing $\Sigma_\infty(Z)$ in Eq. 34 by $\hat{C}_S(Z)/\bar{C}_S = \hat{C}(\tau_S,Z)/\bar{C}(\tau_S)$, for the same cases with $Sc = 1$ and 10 shown in Figure 12. Comparing Figures 12 and 16, we see now higher values of Λ_S ($\Lambda_S \ge 0.9$) in the first local maxima near the disk surface, whereas the values of the global maxima are now lower ($\Lambda_S \le 1.2$), especially for $Sc = 10$. Moreover, the Λ_S drop between the global maximum and the local minimum at $Z = 0$ has been reduced to $\Delta\Lambda_S = 0.3$ in Figure 16, which is much lower than the corresponding Λ_S drop between the first local maximum and the disk surface. A larger concentration gradient within the boundary layer implies a larger reactant consumption at the catalyst surface, and therefore, an increase in mass-transfer efficiency.

The values of the Sherwood number Sh_S, calculated using Eq. 19 with $\eta_S = \eta(\tau_S)$, were fitted to

$$Sh_S = 1.67\, Re^{0.416} Sc^{0.360} \phi^{0.0540} \tag{43}$$

Compared to the fit 32 for the discontinuous reactor, we see now a higher exponent in both the Reynolds number, 0.416 instead of 0.373 and the Schmidt number, 0.360 instead of 0.137. The fact that the Sc exponent in 43 is closer to the theoretical expectation (1/3) supports the notion that the overall mass-transfer process is more boundary layer-controlled. Figure 17a confirms that the fit of Sh_S, with

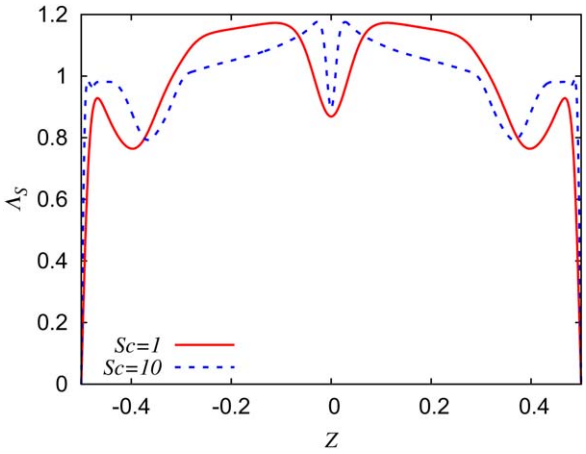

Figure 16. Axial profiles of the radially averaged normalized concentration, Λ_S, obtained with the modified reactor model for $Re=6\times10^4$, $\phi=2000$ and both $Sc=1$ and 10.

The quantity Λ_S is defined in a similar manner as is Λ in Eq. 34 with the concentration $C_S(R,Z)$ replacing the asymptotic concentration $C(\tau_\infty,R,Z)$. [Color figure can be viewed in the online issue, which is available at wileyonlinelibrary.com.]

an average relative error of 0.122, is better than it was for the discontinuous reactor in Figure 11a. Moreover, we see in Figure 17b that the Sh_S values are in the same order of magnitude and, in most cases, surpass the theoretical values given by 33. In particular, for the largest Reynolds number investigated, $Re=10^5$, the Sh_S values for $Sc=10$ plotted in Figure 17 are between 6 and 7 times higher than the corresponding values in Figure11.

Concluding Remarks

We have investigated numerically the mass-transfer problem in a reactor comprising two coaxial, corotating disks in a stationary cylindrical enclosure. The surfaces of the disks are host to a layer of catalyst which promotes a first-order reaction. We have solved the governing equations for the flow field and the resulting concentration field of reactant at a range of Reynolds numbers within $5\times10^3 \le Re \le 10^5$ and Schmidt numbers within $1 \le Sc \le 1000$. We have found that the mass-transfer rate does not follow the expected scaling relation for the Sherwood number, specially at high Schmidt numbers. We attribute this result to the fact that the overall mass transfer in the current system is not controlled by the boundary layer.

An interesting conclusion is that while the reactant concentration drops throughout time, that is, the mass-transfer problem is unsteady, there is a steady relative spatial distribution of reactant. In particular, in all of the present calculations for the discontinuous reactor model, we have found that the normalized concentration field, $\Sigma(\tau,R,Z)=C(\tau,R,Z)/\bar{C}(\tau)$, becomes stationary after a relatively short transient. The same thing happened in our previous work[5] on a natural convection-driven discontinuous reactor in a cubical cavity. The existence of a stationary $\Sigma_\infty(R,Z)$ field may seem surprising at first sight, as the absolute concentration levels in the reactor keep dropping all of the time, but it is in fact a direct consequence of the conservation equations. Under the current assumptions, the molar conservation equation for a chemical species may be written, using a more general vector notation, as

$$\frac{\partial C}{\partial \tau} = -ReSc(\mathbf{U}\cdot\nabla)C + \nabla^2 C \tag{44}$$

We can now introduce the Σ definition 31 into Eq. 44

$$\bar{C}\left(\frac{\partial \Sigma}{\partial \tau}\right) + \Sigma\left(\frac{\partial \bar{C}}{\partial \tau}\right) = -\bar{C}ReSc(\mathbf{U}\cdot\nabla)\Sigma + \bar{C}\nabla^2\Sigma \tag{45}$$

In the present problem, boundary conditions for Eq. 45 would be the equivalent to Eqs. 15 and 16 with Σ in place of C

$$\frac{\partial \Sigma}{\partial Z} = \pm\phi\Sigma \quad \text{at} \quad Z = \mp\frac{1}{2} \tag{46}$$

$$\frac{\partial \Sigma}{\partial R} = 0 \quad \text{at} \quad R = \gamma, 1 \tag{47}$$

A stationary solution, $\Sigma_\infty(R,Z)$, would, therefore, be governed by

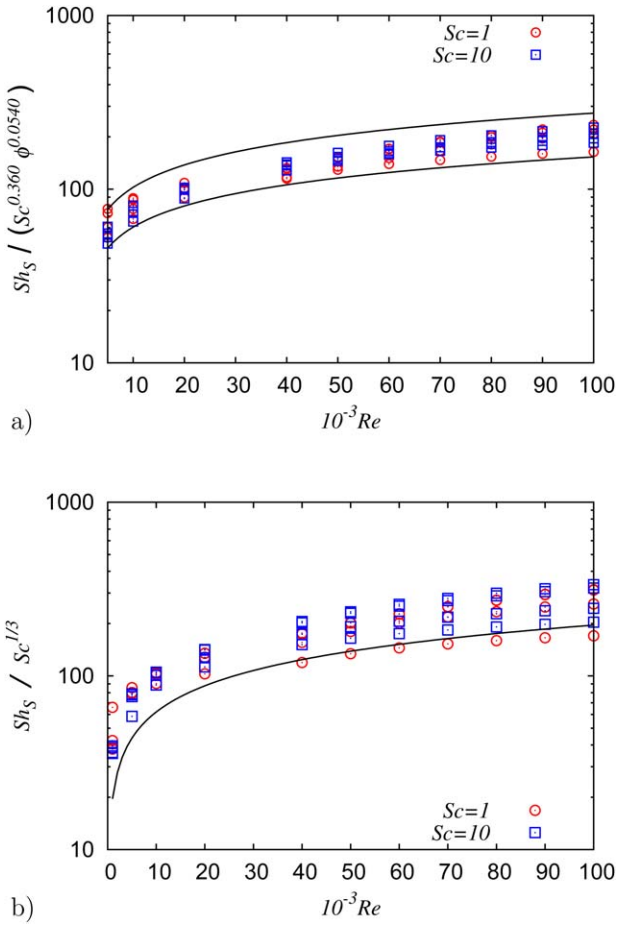

Figure 17. Variation with Re of the predicted values of the Sherwood number, Sh_S, for all of the calculations of the modified reactor model.

In (a), Sh_S is divided by $Sc^{0.360}\phi^{0.0540}$; the two solid lines denote the boundaries of the 95% confidence interval for the fit. In (b), Sh_S is divided by $Sc^{1/3}$ instead and the theoretical boundary-layer prediction, Eq. 33, is plotted with a solid line. In both plots, circles and squares, respectively, denote the results obtained with $Sc=1$ and 10. [Color figure can be viewed in the online issue, which is available at wileyonlinelibrary.com.]

$$-ReSc(\mathbf{U}\cdot\nabla)\Sigma_\infty+\nabla^2\Sigma_\infty=\Sigma_\infty\left(\frac{1}{\bar{C}}\frac{\partial\bar{C}}{\partial\tau}\right)_{\tau=\tau_\infty}=\Sigma_\infty\Gamma_\infty(\Sigma_\infty) \tag{48}$$

where as shown by Eq. 36, $\Gamma_\infty=-2\phi\eta_\infty/S^2$ for the present problem. If the tau–Galerkin spatial discretization is applied to Eqs. 46–48, it is not difficult to see that a set of quadratic equations for the unknown coefficients, **c**, would be obtained. Thus, solving such a system of nonlinear equations would be an alternative method, instead of advancing in time the ODE system 26, to obtain the stationary Σ_∞ (and subsequently $\eta_\infty=\hat{\Sigma}_\infty(\pm1/2)$ on account of 17).

From a physical viewpoint, the nonlinear term in the right hand side of Eq. 48 provides a continuous rate of generation for Σ_∞, which by means of an overall molar balance such as 35 equates to the overall rate of reaction at the catalytic surface. Note that from definition 31, the value of the volume-averaged Σ_∞ is equal to one. Thus, $\Sigma(\tau,R,Z)$ provides the spatial distribution of $C(\tau,R,Z)$, whereas the time evolution of $\bar{C}(\tau)$ tells us how fast the mean concentration levels are dropping. In the present problem, after an initial transient $\Sigma(\tau,R,Z)$ becomes always stationary, and therefore, $\Sigma_\infty(R,Z)$ provides an snapshot of the spatial distribution of reactant.

Note that Eq. 48 is applicable not only to any discontinuous reactor geometry but also is also independent of the particular type of kinetic law assumed. If a nonlinear reaction at the disk surfaces was considered then Γ_∞ would be a highly nonlinear function of the unknown coefficients (and there might be molar balances for several chemical species, not just one). The resulting system of nonlinear equations might or might not have one or multiple solutions for Σ_∞. When such stationary solutions existed, it would be challenging to investigate their stability properties and bifurcation diagrams as a function of the problem parameters and/or kinetic constants.

Acknowledgments

The financial support received from the DGIC project CTQ2008-04857/PPQ and from the CIRIT "Programa de Groups de Recerca Consolidats de la Generalitat de Catalunya" (2009SGR-1529) are gratefully acknowledged.

Literature Cited

1. Yu P, Lee TS, Zeng Y, Low HT. Effect of vortex breakdown on mass transfer in a cell culture bioreactor. *Mod Phys Lett B*. 2005;19:1543–1546.
2. Zeng Y, Lee TS, Yu P, Low HT. Numerical study of mass transfer coefficient in a 3D flat-plate rectangular microchannel bioreactor. *Int Commun Heat Mass*. 2007;34:217–224.
3. Al-Shannag M, Al-Qodah A, Herrero J, Humphrey JAC, Giralt F. Using a wall-driven flow to reduce the external mass-transfer resistance of a bio-reaction system. *Biochem Eng J*. 2008;39:554–565.
4. Al-Shannag M. Mass transport enhancement in annular-shaped lid-driven bioreactor. *Bioproc Biosyst Eng*. 2012;35(6):875–884.
5. Gonzalez-Hidalgo CT, Herrero J, Puigjaner D. Mixing intensification by natural convection with application to a chemical reactor design. *Chem Eng J*. 2012;200–202:506–520.
6. Drumm C, Tiwari S, Kuhnert J, Bart HJ. Finite pointset method for simulation of the liquid–liquid flow field in an extractor. *Comput Chem Eng*. 2008;32(12):2946–2957.
7. Drumm C, Attarakih MM, Bart HJ. Coupling of CFD with DPBM for an RDC extractor. *Chem Eng Sci*. 2009;64(4):721–732.
8. Francis P, Martinez DM, Taghipour F, Bowen BD, Haynes CA. Optimizing the rotor design for controlled-shear affinity filtration using computational fluid dynamics. *Biophys Chem*. 2006;95:1027–1217.
9. Zhang P, Wei H, Cong G, Hu W, Fan H, Wu J, Zhu Q, Liu X. Effects of disk rotation rate on the growth of ZnO films by low-pressure metal-organic chemical vapor deposition. *Thin Solid Films*. 2008;516:925–928.
10. Meeuwse M, van der Schaaf J, Kuster BFM, Schouten JC. Gas–liquid mass transfer in a rotor-stator spinning disc reactor. *Chem Eng Sci*. 2010;65(1):466–471.
11. Meeuwse M, Lempers S, van der Schaaf J, Schouten J. Liquid-solid mass transfer and reaction in a rotor–stator spinning disc reactor. *Ind Eng Chem Res*. 2010;49:10751–10757.
12. Visscher F, van der Schaaf J, de Croon MHJM, Schouten JC. Liquid–liquid mass transfer in a rotor-stator spinning disc reactor. *Chem Eng J*. 2012;185:267–273.
13. Leon MA, Maas RJ, Bieberle A, Schubert M, Nijhuis TA, van der Schaaf J, Hampel U, Schouten JC. Hydrodynamics and gas-liquid mass transfer in a horizontal rotating foam stirrer reactor. *Chem Eng J*. 2013;217:10–21.
14. Belfiore LA, Bonani W, Leoni M, Belfiore CJ. Stress-sensitive nutrient consumption via steady and non-reversing dynamic shear in continuous-flow rotational bioreactors. *Biophys Chem*. 2009;141(2–3):140–152.
15. Belfiore LA. Dynamic shear in continuous-flow rotating-disk catalytic reactors with stress-sensitive kinetics based on Curie's theorem in non-equilibrium thermodynamics. *Chem Eng Sci*. 2010;65(2):680–691.
16. Abrahamson SD, Eaton JK, Koga DJ. The flow between shrouded corotating disks. *Phys Fluids A*. 1989;1(2):241–251.
17. Schuler CA, Usry W, Weber B, Humphrey JAC, Greif R. On the flow in the unobstructed space between shrouded corotating disks. *Phys Fluids A*. 1990;2:3291–3306.
18. Humphrey JAC, Schuler CA, Iglesias I. Analysis of viscous dissipation in disk storage-systems and similar flow configurations. *Phys Fluids A*. 1992;4(7):1415–1427.
19. Radel VS, Szeri AZ. Symmetry breaking bifurcation in finite disk flow. *Phys Fluids*. 1997;9(6):1650–1656.
20. Iglesias I, Humphrey JAC. Two- and three-dimensional laminar flows between disks co-rotating in a fixed cylindrical enclosure. *Int J Numer Meth Eng*. 1998;26(5):581–603.
21. Herrero J, Giralt F, Humphrey JAC. Influence of the geometry on the structure of the flow between a pair of corotating disks. *Phys Fluids*. 1999;11:88–96.
22. Randriamampianina A, Schieste R, Wilson M. Spatio-temporal behaviour in an enclosed corotating disk pair. *J Fluid Mech*. 2001;434:39–64.
23. Miura T, Mizushima J. Transitions of axisymmetric flow between two corotating disks in an enclosure. *Fluid Dyn Res*. 2007;39(1–3):193–208.
24. Mizushima J, Sugihara G, Miura T. Two modes of oscillatory instability in the flow between a pair of corotating disks. *Phys Fluids*. 2009;21:014101–1–15.
25. Koschmieder EL. *Bénard cells and Taylor vortices*. Cambridge: Cambridge University Press, 1993.
26. Boyd JP. *Chebyshev and Fourier spectral methods*. Mineola, New York: Dover Publications, 2001.
27. Lopez JM, Shen J. An efficient spectral-projection method for the Navier-Stokes equations in cylindrical geometries. I. Axisymmetric cases. *J Comput Phys*. 1998;139:308–326.
28. Lopez JM, Marques F, Shen J. Complex dynamics in a short annular container with rotating bottom and inner cylinder. *J Fluid Mech*. 2004;501:327–354.
29. Butcher JC. *Numerical methods for ordinary differential equations*. New York: Wiley, 2003.
30. Dongarra J, Croz JD, Hammarling S, Hanson RJ. An extended set of FORTRAN basic linear algebra subroutines. *ACM T Math Software*. 1988;14:1–17.
31. Dongarra J, Croz JD, Duff I, Hammarling S. A set of level 3 basic linear algebra subprograms. *ACM T Math Software*. 1990;16:1–17.
32. Bird RB, Stewart WE, Lightfoot EN. *Transport phenomena*, 2nd ed. New York: Wiley, 2002.

APPENDIX

The aim of this appendix is to give some details of the tau–Galerkin method used to discretize the governing equations. We start with the mass-transfer conservation Eqs. 14–16. Note that these equations can be written in a compact form as

$$\frac{\partial C}{\partial \tau}-\nabla^2 C+ReSc\nabla\cdot(C\mathbf{V})=0 \tag{49}$$

$$\frac{\partial C}{\partial Z}(R,\pm 1/2)\pm\phi C(R,\pm 1/2)=0 \tag{50}$$

$$\frac{\partial C}{\partial R}(\gamma,Z)=0 \tag{51}$$

$$\frac{\partial C}{\partial R}(1,Z)=0 \tag{52}$$

where

$$\nabla=\left(\frac{\partial}{\partial R},\frac{1}{S}\frac{\partial}{\partial Z}\right)$$

$$\nabla^2=\left(\frac{1}{R}\frac{\partial}{\partial R}\left(R\frac{\partial}{\partial R}\right)+\frac{1}{S^2}\frac{\partial^2}{\partial Z^2}\right)$$

$$\mathbf{V}=(U,W)$$

Let us first recall that, as it was discussed above only solutions with velocity fields symmetric with respect the plane $Z=0$ were obtained in this work. As a consequence, only even functions in Z are considered when the concentration is expanded in terms of the basis function. Thus, the concentration expansion is written as

$$C(\tau,R,Z)=\sum_{i=0}^{N_R}\sum_{j=0}^{N_Z/2}c_{i2j}(\tau)T_i(R^*)T_{2j}(Z^*) \tag{53}$$

where $R^*=2[(R-\gamma)/(1+\zeta-\gamma)-1/2], Z^*=2Z$ and T_i are the Chebyshev polynomials. In addition, by substituting Eq. 22 in Eqs. 7 and 8 and replacing the basis functions f_i by the corresponding linear combination of Chebyshev polynomials, the velocity vector $\mathbf{V}$ takes the form

$$\mathbf{V}(\tau,R,Z)=\begin{pmatrix}U(\tau,R,Z)\\W(\tau,R,Z)\end{pmatrix}=\sum_{i=0}^{N_{R,\Psi}}\sum_{j=0}^{N_{Z,\Psi}}\varphi_{ij}(\tau)\begin{pmatrix}T_i(R^*)T_j'(Z^*)\\T_i'(R^*)T_j(Z^*)\end{pmatrix} \tag{54}$$

The tau–Galerkin method consists in projecting Eq. 49 into the subspace generated by all the basis functions in the concentration expansion except for $T_{N_R-1}(R^*), T_{N_R}(R^*), T_{N_Z-2}(Z^*)$ and $T_{N_Z}(Z^*)$. The basis functions that are not used to project Eq. 49, are used to project boundary conditions 50–52. Therefore, application of the tau–Galerkin method converts Eqs. 49–52 into the following equations

$$\left\langle\frac{\partial C}{\partial Z},T_iT_{2j}\right\rangle-\langle\nabla^2 C,T_iT_{2j}\rangle+ReSc\langle\nabla\cdot(C\mathbf{V}),T_iT_{2j}\rangle=0 \tag{55}$$

with $i=0,\ldots,N_R-2$ and $j=0,\ldots,N_Z/2-2$

$$\left\langle\frac{\partial C}{\partial Z}(R,1/2),T_iT_{2j}(1)\right\rangle+\langle\phi C(R,1/2),T_iT_{2j}(1)\rangle=0 \tag{56}$$

with $i=0,\ldots,N_R-2$ and $j=N_Z/2$

$$\left\langle\frac{\partial C}{\partial Z}(R,-1/2),T_iT_{2j}(-1)\right\rangle-\langle\phi C(R,-1/2),T_iT_{2j}(-1)\rangle=0$$

with $i=0,\ldots,N_R-2$ and $j=N_Z/2-1$ (57)

$$\left\langle\frac{\partial C}{\partial R}(\gamma,Z),T_i(-1)T_{2j}\right\rangle=0 \tag{58}$$

with $i=N_R$ and $j=0,\ldots,N_Z/2$

$$\left\langle\frac{\partial C}{\partial R}(1+\zeta,Z),T_i(1)T_{2j}\right\rangle=0 \tag{59}$$

with $i=N_R-1$ and $j=0,\ldots,N_Z/2$

where $\langle\rangle$ represents the inner product. Note that due to the symmetries of the problem Eq. 56 is equivalent to Eq. 57.

Integrals involved in the calculation of the inner products in Eqs. 55–59 are of the type

$$\int_{-1}^{1}R^*T_iT_j\omega(R^*)dR^*,\quad\int_{-1}^{1}T_iT_j\omega(Z^*)dZ^*,\quad\int_{-1}^{1}T_i'T_j\omega(R^*)dR^*,$$
$$\int_{-1}^{1}R^*T_i''T_j\omega(R^*)dR^*,\quad\int_{-1}^{1}T_i''T_j\omega(Z^*)dZ^*,\quad\int_{-1}^{1}T_i'T_jT_kd\omega(R^*)R^*,$$
$$\int_{-1}^{1}T_iT_j'T_k\omega(Z^*)dZ^*,\quad\int_{-1}^{1}T_iT_j'T_k\omega(R^*)dR^*,\quad\int_{-1}^{1}T_i'T_jT_k\omega(Z^*)dZ^*,$$
$$A\int_{-1}^{1}e^{-\frac{Z^{*2}}{\sigma^2}}T_i\omega(Z^*)dZ^* \tag{60}$$

where ω is the Chebyshev weight function, $\omega(x)=(1-x^2)^{-1/2}$. Once the inner products in Eqs. 55–59 are calculated, these equations can be written in the matricial form as

$$(\mathbf{B}\quad\mathbf{B_b})\begin{pmatrix}\dot{\mathbf{c}}\\\dot{\mathbf{c}}_\mathbf{b}\end{pmatrix}=(\mathbf{L}\quad\mathbf{L_b})\begin{pmatrix}\mathbf{c}\\\mathbf{c}_\mathbf{b}\end{pmatrix} \tag{61}$$

$$(\mathbf{D}\quad\mathbf{D_b})\begin{pmatrix}\mathbf{c}\\\mathbf{c}_\mathbf{b}\end{pmatrix}=\mathbf{J_b} \tag{62}$$

Let us define $DS=(N_R-1)(N_Z/2-1)$ and $DB=N_Z+2N_R$. Then, $\mathbf{B}$ and $\mathbf{L}$ are square matrices of dimension DS, $\mathbf{B_b}$ and $\mathbf{L_b}$ are matrices of dimension (DS×DB), $\mathbf{D}$ is a matrix of dimension (DB×DS), and $\mathbf{D_b}$ is a square matrix of dimension DB. The flux entering the reactor through the boundaries in the modified model is represented by the vector $\mathbf{J_b}$ whose dimension is (DB). Whereas the coefficients c_{i2j} in the concentration expansion 25 with $i=0,\ldots,N_R-2$ and $j=0,\ldots,N_Z/2-2$ are contained in the vector $\mathbf{c}$ of dimension DS, the vector $\mathbf{c_b}$, whose dimension is DB, contains those coefficients with either $i=0,\ldots,N_R-2$ and $j=N_Z/2-1,N_Z/2$ or $i=N_R-1,N_R$, and $j=0,\ldots,N_Z/2$.

Isolating $\mathbf{c_b}$ from Eq. 62 and inserting the result into Eq. 61 leads to the ODE

$$\hat{\mathbf{B}}\dot{\mathbf{c}}=\hat{\mathbf{L}}\mathbf{c}+\hat{\mathbf{A}} \tag{63}$$

where

$$\hat{\mathbf{B}}=\mathbf{B}-\mathbf{B_b}\mathbf{D_b}^{-1}\mathbf{D} \tag{64}$$

$$\hat{\mathbf{L}}=\mathbf{L}-\mathbf{L_b}\mathbf{D_b}^{-1}\mathbf{D} \tag{65}$$

$$\hat{\mathbf{A}}=\mathbf{L_b}\mathbf{D_b}^{-1}\mathbf{J_b} \tag{66}$$

Equation 63 is advanced in time by means of a second-order implicit backward-differencing scheme (BDF2). Note that once the value of $\mathbf{c}(\tau)$ is obtained, $\mathbf{c_b}(\tau)$ can easily be obtained from Eq. 62.

The steady-state version of the momentum conservation Eqs. 1–4 is also discretized by means of a tau–Galerkin method. The discretization procedure reduces these equations to a nonlinear system of algebraic equations that, adopting the summation convention indices, can be written as

$$L_{ji}d_i + Q_{jin}d_i d_n = 0 \tag{67}$$

In Eq. 67, the elements of the vector $\mathbf{d}=(d_1,\ldots,d_K)$ are the unknowns, that is, the coefficients in expansions 22 and 23. The matrices with components L_{ji} and Q_{jin} contain, respectively, the coefficients of the linear and nonlinear terms resulting from the projection of the velocity governing equations into the space generated by the basis functions. It should be noted that the projection of the pressure gradient onto the basis is analytically zero which means that the pressure gradient is not present in the discretized equations. This is so because of two reasons: the formulation of the velocity in terms of a scalar potential function (see Eqs. 7 and 8) and the choice of basis functions in the expansion of the potential function in 22 that makes boundary conditions 5 and 6 for U and W be automatically fulfilled. The nonlinear discretized Eqs. 67 were solved by means of an iterative Newton method.

Manuscript received June 30, 2014, and revision received Oct. 3, 2014.